Available online at www.sciencedirect.com
ScienceDirect
Planetary and Space Science 55 (2007) 1896–1935
Planetary and Space Science
www.elsevier.com/locate/pss

DISR imaging and the geometry of the descent of the Huygens probe within Titan's atmosphere

Erich Karkoschka[a,*], Martin G. Tomasko[a], Lyn R. Doose[a], Chuck See[a], Elisabeth A. McFarlane[a], Stefan E. Schröder[b], Bashar Rizk[a]

[a]*Lunar and Planetary Laboratory, University of Arizona, Tucson, AZ 85721-0092, USA*
[b]*Max-Planck-Institut für Sonnensystemforschung, 37191 Katlenburg-Lindau, Germany*

Accepted 13 April 2007
Available online 27 April 2007

Abstract

The Descent Imager/Spectral Radiometer (DISR) provided 376 images during the descent to Titan and 224 images after landing. Images of the surface had scales between 150 m/pixel and 0.4 mm/pixel, all of which we assembled into a mosaic. The analysis of the surface and haze features in these images and of other data gave tight constraints on the geometry of the descent, particularly the trajectory, the tip and tilt, and the rotation of the Huygens probe.

Huygens moved on average in the direction of 2° north of east from 145 to 50 km altitude, turning to 5° south of east between 30 and 20 km altitude, before turning back to east. At 6.5 km altitude, it reversed to WNW, before reversing back to SE at 0.7 km altitude.

At first, Huygens was tilting slowly by up to 15° as expected for a descent through layers of changing wind speeds. As the winds calmed, tilts decreased. Tilts were approximately retrieved throughout the main-parachute phase, but only for 160 specific times afterwards. Average swing rates were 5°/s at high and low altitudes, but 13°/s between 110 and 30 km altitude. Maximum swing rates were often above 40°/s, far above the design limit of 6°/s, but they caused problems only for a single component of DISR, the Sun Sensor. The excitation of such high swing rates on the stabilizer parachute is not fully understood.

Before the parachute exchange, the rotational rate of Huygens smoothly approached the expected equilibrium value of 3 rotations per vertical kilometer, although clockwise instead of counterclockwise. Starting at 40 s after the parachute exchange until landing, Huygens rotated erratically. Long-term averages of the rotational rate varied between 2.0 and 4.5 rotations/km. On time scales shorter than a minute, some 100 strong rotational accelerations or decelerations created azimuthal irregularities of up to 180°, which caused DISR to take most exposures at random azimuths instead of pre-selected azimuths. Nevertheless, we reconstructed the azimuths throughout the 360 rotations during the descent and for each of some 3500 DISR exposures with a typical accuracy near 2°.

Within seconds after landing, the parachute moved into the field of view of one of the spectrometers. The observed light curve indicated a motion of the parachute of 0.3 m/s toward the SSE. DISR images indicated that the probe did not penetrate into the surface, assuming a level ground. This impact of Huygens must have occurred on major rocks or some elevated area. The unexpected raised height increases ice-rock sizes by 40% with respect to estimations made in 2005 [Tomasko, M.G., Archinal, B., Becker, T., Bézard, B., Bushroe, M., Combes, M., Cook, D., Coustenis, A., de Bergh, C., Dafoe, L.E., Doose, L., Douté, S., Eibl, A., Engel, S., Gliem, F., Grieger, B., Holso, K., Howington-Kraus, E., Karkoschka, E., Keller, H.U., Kirk, R., Kramm, R., Küppers, M., Lanagan, P., Lellouch, E., Lemmon, M., Lunine, J., McFarlane, E., Moores, J., Prout, G.M., Rizk, B., Rosiek, M., Rueffer, P., Schröder, S.E., Schmitt, B., See, C., Smith, P., Soderblom, L., Thomas, N., West, R., 2005. Rain, winds and haze during the Huygens probe's descent to Titan's surface. Nature 438, 765–778]. During the 70-min surface phase, the tilt of Huygens was 3°, changing by a small fraction of a degree. The apparent horizon looking south to SSW from the landing site was 1–2° above the theoretical horizon, sloping by 1° up to the left (east). Our best guess puts the horizon as a 1–2 m high hill in 30–50 m distance. We detected the refraction from warm, rising air bubbles above our illuminated spot. Bright, elongated, cm-sized objects appear occasionally on the surface. If real, they could be rain drop splashes or fluffy particles blown across Titan's surface.

Keywords: Titan

*Corresponding author. Tel.: +1 520 621 3994; fax: +1 520 621 4933.
E-mail address: erich@lpl.arizona.edu (E. Karkoschka).

0032-0633/$ - see front matter © 2007 Elsevier Ltd. All rights reserved.
doi:10.1016/j.pss.2007.04.019

1. Introduction

The Descent Imager/Spectral Radiometer (DISR) of the Huygens probe had three imagers, a solar aureole camera with four channels, two visible and two infrared spectrometers, two violet photometers, and a Sun Sensor. During the almost 4-h long operation, some 3500 exposures were taken and received. The value of each exposure is strongly dependent on the knowledge about the position and orientation of the Huygens probe at the time of the exposure. We have analyzed the data of the imagers and several other components in order to constrain the position and orientation of Huygens throughout the descent and after touch down. In this paper, we will focus on the topics which influence the geometry. Further analysis of the DISR data is discussed in companion papers. Some basic facts about the Huygens descent and the DISR camera are described by Tomasko et al. (2005), and they are not repeated here. The Huygens mission is summarized in Lebreton et al. (2005). We use altitude and Mission Time (MT, measured in seconds, s) as descent parameters. DISR started taking data soon after MT 0 near 150 km altitude, and landing occurred at MT 8870.

The position and orientation of Huygens is fully described by three position coordinates and three angular coordinates as functions of time. The goal of this work is to determine these six functions as accurately as possible. While there are different choices of coordinate systems, we will use the altitude, sub-Huygens longitude and latitude, the rotation angle, or more accurately the azimuth of the z-axis of Huygens, the pitch angle, and the roll angle. We measure longitudes positively toward the east, azimuths clockwise from north or from the solar azimuth. A positive pitch angle means DISR is looking down, and a positive roll angle means that Huygens rolled clockwise when viewed in the direction of the z-axis of Huygens, which is the main viewing direction of DISR (cf. Fig. 12 in Tomasko et al., 2002).

One of the six functions, the altitude, was taken from the results of the Huygens Descent Working Group (DTWG) (Kazeminejad et al., 2007), which is mostly based on the pressure and temperature measurements from the Huygens Atmospheric Structure Instrument (HASI) (Fulchignoni et al., 2005) and the mean molecular weight measurements by the Gas Chromatograph Mass Spectrometer (GCMS) (Niemann et al., 2005). All our data were found to be consistent with their determination. Some of our data are quite sensitive to altitudes, such as the image scales in an image pair of the same feature, but taken from different altitudes. If some altitude data by Kazeminejad et al. were off by more than a few percent, we could have detected it, at least below 40 km altitude. This leaves five functions to be determined in this work.

We start with the description of the calibration of the imagers (Section 2) and the creation of the surface mosaic (Section 3) and the sky mosaic (Section 4). Following are discussions about other data to constrain the rotation of Huygens (Section 5) and the location of the descent (Section 6), and the Sun Sensor data (Section 7). In Section 8, we discuss the geometry after landing. Section 9 gives information about the wind at the surface. A discussion (Section 10) summarizes our results.

2. Calibration of the DISR imagers

2.1. The imagers

The three DISR imagers are the Side Looking Imager (SLI), Medium Resolution Imager (MRI), and High Resolution Imager (HRI). The SLI images a 25° wide area between 45° and 96° nadir angle. Its 128 × 256 pixel array has a scale of 0.2°/pixel. The MRI images a 21° wide area between 16° and 46° nadir angle. Its 176 × 256 pixel array has a scale of 0.12°/pixel. The HRI images a 10° wide area between 7° and 22° nadir angle. Its 160 × 256 pixel array has a scale of 0.06°/pixel. All three imagers have the same central azimuth. The whole area between 7° and 96° nadir angle can be imaged with an azimuthal spacing between exposures of about 30° (cf. Table I and Fig. 9 in Tomasko et al., 2002). The timing of all descent exposures (except for seven calibration exposures) and the first exposure after landing is listed in Table 1, which also contains the geometry parameters derived in this investigation.

2.2. Image distortion and relative geometry

The distortion of the three imagers was measured in the laboratory by two methods. The first method was taking one image with each imager of a prepared, flat target containing some 20 parallel horizontal and vertical lines with constant line spacing. We applied a measuring routine to the images which centered in on all intersections of lines to sub-pixel accuracy. We fitted all coordinates with an automated routine by bi-cubic polynomials of the x- and y-positions to 0.1 pixel rms (root mean square) accuracy. Thus, our first method gave us the distortion of each imager except for six constants: the nadir angle and azimuth of the image center in the Huygens coordinate frame, the image scale, the rotation of an image with respect to the vertical direction, and two constants due to the angle between the optical axis and the normal of the target. In the laboratory, this angle was aligned to be zero as close as possible, but the analysis of the images retrieved these angles to better accuracy than could be measured directly.

These six constants were determined with our second method. We mounted the camera on an alt-azimuth mount with decoders and illuminated each imager with a resting point source. For each imager, we took images for some 30 combinations of azimuth and elevation angle. Our measurements of the locations of the imaged point source could only be explained by two imperfections of the decoders: we found that the azimuth encoder had a backlash of 0.04° and a periodic error of the same

Table 1
Image parameters

MT	Altit	X	Y	Pitch	Roll	Azim	SMH
143.58	142.77	−157.01	−3.27	−8.2	9.1	315.6	S
146.60	142.64	−156.72	−3.26	−13.1	5.9	226.5	SMH
157.45	142.11	−155.68	−3.21	−8.0	0.5	269.3	H
169.45	141.45	−154.51	−3.16	−6.4	8.6	292.8	S
180.26	140.87	−153.44	−3.12	−0.2	4.8	353.8	MH
202.03	139.79	−151.31	−3.03	−0.3	−7.3	143.2	S
204.77	139.66	−151.04	−3.02	2.0	0.5	71.5	MH
216.68	139.09	−149.87	−2.97	−2.6	−0.3	138.5	S H
229.99	138.41	−148.57	−2.92	2.2	3.9	181.3	S H
255.99	137.17	−146.02	−2.82	−0.2	0.2	314.5	H
262.31	136.87	−145.40	−2.79	6.9	−7.1	180.7	S
279.84	136.04	−143.67	−2.72	0.0	−0.1	174.3	MH
285.24	135.78	−143.13	−2.70	2.8	−1.2	68.4	S
306.26	134.82	−141.05	−2.61	−2.6	5.3	31.5	SM
309.70	134.66	−140.72	−2.60	0.3	−0.5	328.4	M
320.59	134.16	−139.64	−2.55	−5.6	5.1	145.5	SMH
333.18	133.53	−138.41	−2.50	−3.3	−4.3	306.6	S
343.83	133.05	−137.37	−2.46	−3.8	10.3	150.5	SMH
356.28	132.47	−136.15	−2.41	−1.5	−0.6	342.1	S H
367.85	131.93	−135.03	−2.36	−5.4	12.3	197.9	S
383.16	131.29	−133.59	−2.31	2.4	−2.0	23.8	SM
391.23	130.91	−132.84	−2.27	8.2	−5.3	298.5	S H
401.39	130.44	−131.91	−2.24	2.3	−7.8	197.0	S
430.98	129.20	−129.22	−2.12	−0.4	0.3	297.1	M
784.78	115.34	−95.82	−0.75	−6.4	6.6	82.1	SMH
831.20	113.69	−92.38	−0.61	−9.0	−16.0	8.2	S H
836.99	113.48	−91.97	−0.59	4.6	−0.2	96.3	S H
846.37	113.15	−91.33	−0.57	10.6	7.5	242.6	S
867.93	112.40	−89.92	−0.51	12.0	4.9	234.1	MH
873.60	112.21	−89.57	−0.50	−4.9	−16.0	330.0	S
882.86	111.91	−88.99	−0.47	−5.2	0.5	129.7	M
893.64	111.54	−88.30	−0.44	2.6	−3.4	318.7	M
907.53	111.00	−87.36	−0.41	−12.0	−3.3	214.5	MH
917.53	110.60	−86.74	−0.38	−3.4	−8.5	43.5	S H
928.74	110.06	−86.07	−0.35	4.3	−0.1	267.5	H
941.11	109.36	−85.36	−0.32	−5.5	−5.7	181.6	S
955.72	108.44	−84.52	−0.29	−1.0	2.3	152.7	M
1408.83	80.259	−65.717	0.486	−3.0	−4.2	42.2	S H
1411.71	80.117	−65.676	0.488	1.5	3.3	180.6	S
1433.36	79.082	−65.396	0.499	−4.5	4.3	130.3	M
1437.01	78.910	−65.354	0.501	4.8	−3.5	302.7	MH
1447.48	78.414	−65.248	0.505	−6.0	−1.6	77.1	S H
1458.10	77.908	−65.159	0.509	6.1	0.3	208.8	S
1469.49	77.402	−65.082	0.512	−0.4	−4.2	2.7	MH
1480.66	76.906	−65.019	0.515	3.5	10.0	140.1	S
1493.82	76.322	−64.951	0.518	0.3	−2.1	347.7	MH
1517.59	75.279	−64.841	0.523	0.6	0.0	263.9	MH
1529.00	74.786	−64.793	0.525	6.4	0.7	13.3	S
1957.47	60.524	−54.477	0.884	8.7	−2.9	118.6	SMH
2095.63	57.241	−49.487	1.039	2.3	2.3	15.8	S H
2122.82	56.637	−48.548	1.065	1.4	2.4	283.5	SM
2126.01	56.568	−48.440	1.068	0.0	−1.5	358.3	MH
2148.51	56.081	−47.683	1.089	−0.6	1.9	170.6	S
2152.85	55.988	−47.539	1.093	−0.1	2.3	266.0	SM
2162.64	55.780	−47.216	1.101	−0.9	0.4	109.3	M
2173.52	55.549	−46.860	1.110	0.2	−0.8	341.4	M
2184.68	55.314	−46.494	1.120	0.5	0.5	223.8	M
2195.83	55.079	−46.132	1.129	−0.6	0.2	102.3	MH
2210.07	54.786	−45.673	1.141	−4.0	−3.5	41.1	S H
2225.98	54.461	−45.161	1.153	4.1	−1.3	340.8	H
2563.95	48.272	−35.465	1.325	−1.3	0.0	178.5	SMH
2974.12	42.120	−26.208	1.320	1.9	−2.9	229.6	S
2977.15	45.079	−26.149	1.319	−5.0	−6.2	276.5	SMH

Table 1 (*continued*)

MT	Altit	*X*	*Y*	Pitch	Roll	Azim	SMH
3011.10	41.622	−25.504	1.312	−0.3	−3.9	105.5	SM
3016.80	41.545	−25.397	1.311	−3.4	−3.8	197.6	M
3025.34	41.430	−25.235	1.309	3.1	4.4	332.4	SM
3043.14	41.193	−24.903	1.305	−1.4	−10.0	252.7	SMH
3059.77	40.974	−24.596	1.300	1.5	0.1	158.6	S H
3066.42	40.887	−24.478	1.299	−2.1	−3.6	268.1	H
3074.49	40.781	−24.336	1.296	0.6	−0.9	34.4	S
3093.35	40.534	−24.003	1.291	−5.2	1.0	317.6	MH
3655.21	33.977	−15.655	1.073	−0.9	1.1	258.8	M
3658.50	33.943	−15.615	1.071	1.0	0.0	304.8	M
3681.62	33.701	−15.336	1.059	−0.5	−3.6	271.5	M
3684.94	33.667	−15.296	1.058	1.1	−1.5	319.2	M
3696.57	33.545	−15.158	1.052	3.8	0.2	117.9	M
3706.61	33.437	−15.040	1.046	0.3	−2.0	264.9	M
3719.96	33.298	−14.885	1.039	−5.4	−2.8	91.1	M
3729.25	33.202	−14.779	1.034	−1.1	−2.6	219.2	M
3742.74	33.063	−14.629	1.027	5.4	2.4	48.2	MH
3752.89	32.959	−14.515	1.022	−2.7	0.1	189.1	S
3768.16	32.805	−14.340	1.013	1.8	0.9	55.3	SM
3792.06	32.564	−14.073	1.000	1.8	−4.3	12.3	MH
4340.15	27.443	−9.099	0.658	1.8	3.2	175.5	M
4344.15	27.408	−9.070	0.655	1.5	−1.7	219.8	M
4366.22	27.217	−8.914	0.640	−2.6	1.0	101.8	SM
4370.25	27.183	−8.886	0.637	3.2	−4.0	142.4	MH
4382.33	27.081	−8.801	0.628	−1.0	−1.6	261.0	S H
4396.65	26.956	−8.701	0.618	−2.8	1.1	51.0	S H
4402.65	26.904	−8.659	0.614	1.1	−0.4	115.5	S H
4422.93	26.729	−8.520	0.599	−2.3	4.6	331.9	S
4429.09	26.675	−8.477	0.595	1.6	−0.9	34.6	M
4449.60	26.501	−8.338	0.580	0.6	1.8	254.6	MH
4457.81	26.429	−8.285	0.574	0.4	−1.7	344.1	H
4493.18	26.130	−8.053	0.548	−1.3	2.7	25.7	S
4858.38	23.191	−5.789	0.276	−2.0	2.0	286.1	MH
4863.93	23.147	−5.761	0.272	−0.9	−5.3	346.2	S H
4886.32	22.976	−5.645	0.254	−1.2	1.1	221.0	S
4894.79	22.912	−5.600	0.248	2.5	2.2	308.4	MH
4903.31	22.847	−5.556	0.241	−2.7	3.2	35.1	S
4911.81	22.781	−5.512	0.235	−0.2	−2.4	120.4	SM
4934.45	22.607	−5.394	0.217	−1.6	0.5	344.6	MH
4940.10	22.564	−5.364	0.212	2.3	−1.9	35.9	S
4948.63	22.500	−5.318	0.206	2.0	−2.7	104.1	MH
4976.89	22.287	−5.163	0.184	2.8	−4.6	284.4	S
4985.39	22.222	−5.118	0.178	−2.0	0.2	333.7	SM
5025.22	21.922	−4.914	0.149	1.3	−3.2	276.7	MH
5199.31	20.637	−4.150	0.033	−1.8	−1.8	190.5	S H
5205.08	20.595	−4.126	0.029	−1.3	0.5	251.5	SH
5225.38	20.451	−4.041	0.017	−2.1	0.3	97.0	S
5237.01	20.370	−3.994	0.011	−2.2	1.5	201.3	M
5242.85	20.329	−3.969	0.007	2.0	−4.5	253.9	M
5251.68	20.265	−3.936	0.002	−0.1	3.2	332.9	MH
5263.25	20.182	−3.887	−0.004	1.2	−0.9	73.6	H
5280.71	20.056	−3.813	−0.014	2.8	−4.1	231.1	H
5289.46	19.994	−3.777	−0.019	4.1	1.9	318.1	S
5301.11	19.912	−3.731	−0.025	2.8	0.4	78.2	SMH
5318.60	19.786	−3.663	−0.034	−1.6	0.5	263.0	S
5327.33	19.724	−3.631	−0.039	−0.9	−0.3	354.0	MH
5728.70	16.980	−2.189	−0.186	−0.6	−3.4	340.0	M
5734.46	16.942	−2.171	−0.187	−0.9	−1.2	34.1	M
5756.60	16.797	−2.099	−0.191	3.8	0.0	241.3	SM
5764.77	16.743	−2.075	−0.193	2.3	−0.4	317.6	MH
5772.96	16.689	−2.050	−0.195	1.8	0.6	31.8	S
5783.76	16.618	−2.016	−0.197	−0.6	−1.0	133.0	SM
5803.19	16.491	−1.955	−0.200	0.2	0.6	324.4	M
5808.77	16.454	−1.938	−0.201	−1.7	−1.7	18.5	MH

Table 1 (*continued*)

MT	Altit	*X*	*Y*	Pitch	Roll	Azim	SMH
5842.97	16.229	−1.831	−0.206	1.1	−0.8	355.3	MH
5875.80	16.014	−1.726	−0.210	−0.5	−4.0	301.8	MH
6069.61	14.782	−1.163	−0.217	1.7	−0.2	330.3	S H
6074.78	14.750	−1.148	−0.217	−1.4	4.7	14.3	S
6095.44	14.618	−1.091	−0.216	2.3	−1.4	210.3	M
6103.19	14.570	−1.069	−0.216	3.4	1.0	283.4	MH
6110.95	14.521	−1.048	−0.215	1.9	0.9	355.4	S
6121.29	14.457	−1.020	−0.214	−0.5	1.4	96.9	MH
6139.47	14.343	−0.975	−0.213	1.3	0.4	279.6	S
6147.34	14.295	−0.956	−0.212	−0.8	−0.9	355.5	MH
6155.17	14.246	−0.934	−0.212	−0.2	−0.9	70.9	H
6181.36	14.085	−0.860	−0.209	1.1	3.8	324.2	S
6207.69	13.924	−0.787	−0.206	0.4	−2.2	202.1	MH
6223.49	13.827	−0.744	−0.204	0.0	−0.7	343.3	S H
6407.22	12.722	−0.317	−0.187	1.7	−2.2	186.9	S
6415.39	12.673	−0.299	−0.186	2.0	1.8	263.5	SMH
6423.57	12.624	−0.282	−0.186	0.3	0.8	339.3	S H
6445.40	12.492	−0.241	−0.184	−0.7	−0.4	177.3	S H
6450.85	12.461	−0.231	−0.183	−0.5	−1.1	224.6	S H
6461.82	12.397	−0.211	−0.183	1.5	−4.4	315.5	S H
6475.53	12.318	−0.184	−0.181	−2.0	1.8	63.9	S
6486.55	12.255	−0.163	−0.181	2.1	−0.5	144.1	M
6497.56	12.190	−0.142	−0.180	0.6	−1.4	224.2	MH
6525.18	12.029	−0.091	−0.178	3.4	−2.8	89.6	H
6533.50	11.980	−0.076	−0.177	−2.7	2.8	154.9	S
6569.52	11.769	−0.012	−0.174	1.6	1.2	108.8	MH
6740.54	10.785	0.250	−0.164	1.0	0.1	76.8	S H
6746.26	10.752	0.258	−0.163	0.1	0.1	122.3	S
6757.70	10.687	0.273	−0.163	0.8	0.9	218.1	MH
6777.74	10.573	0.300	−0.162	−0.8	0.2	24.0	S
6783.50	10.540	0.307	−0.162	−0.8	−0.1	69.3	M
6794.92	10.475	0.322	−0.161	1.3	2.9	159.4	MH
6803.86	10.425	0.332	−0.161	−0.2	1.2	226.3	S
6832.43	10.263	0.367	−0.159	0.0	−0.9	80.5	MH
6841.08	10.216	0.377	−0.159	1.9	2.1	148.5	S
6855.49	10.136	0.393	−0.158	2.3	−1.0	263.1	SM
6869.99	10.055	0.409	−0.157	−0.1	−0.6	24.2	MH
6893.26	9.924	0.435	−0.156	1.9	−2.3	203.9	S
7065.41	8.970	0.589	−0.150	1.5	2.8	206.6	M
7071.34	8.937	0.593	−0.150	2.3	−1.2	248.4	M
7083.23	8.871	0.601	−0.149	−0.9	−0.3	336.0	MH
7110.17	8.722	0.619	−0.149	3.3	1.6	172.7	M
7122.18	8.658	0.628	−0.148	1.9	−0.8	268.6	M
7131.18	8.610	0.633	−0.148	−0.2	−2.0	340.9	MH
7149.16	8.511	0.644	−0.148	0.8	0.4	124.0	S H
7161.18	8.446	0.651	−0.147	2.3	−2.6	219.2	S H
7170.18	8.398	0.656	−0.147	2.2	−3.9	286.3	H
7188.24	8.302	0.666	−0.147	−0.7	−1.0	61.6	S
7200.33	8.236	0.672	−0.147	0.4	0.5	153.8	M
7388.28	7.229	0.738	−0.144	1.4	0.9	87.8	M
7397.56	7.180	0.740	−0.144	3.5	0.5	156.7	MH
7403.75	7.148	0.741	−0.144	0.7	−2.7	200.7	S
7428.49	7.017	0.745	−0.144	0.3	−0.1	16.8	MH
7437.76	6.967	0.747	−0.144	0.2	−0.9	83.0	S
7443.96	6.935	0.748	−0.144	0.2	−0.2	132.2	M
7456.33	6.870	0.749	−0.144	0.5	−1.1	231.4	M
7484.38	6.723	0.751	−0.144	0.4	−0.2	66.3	M
7490.67	6.690	0.752	−0.144	0.7	−0.4	109.9	MH
7525.06	6.511	0.753	−0.144	0.1	0.1	335.6	MH
7534.43	6.463	0.753	−0.144	0.7	−0.5	39.4	S H
7719.49	5.510	0.729	−0.136	−0.7	0.9	25.3	S H
7735.44	5.429	0.725	−0.134	0.2	1.9	138.0	S
7741.82	5.396	0.723	−0.134	0.6	−0.8	181.4	MH
7751.40	5.348	0.720	−0.133	0.9	1.0	245.6	S

Table 1 (*continued*)

MT	Altit	*X*	*Y*	Pitch	Roll	Azim	SMH
7760.98	5.300	0.717	−0.132	1.1	−0.6	309.3	SMH
7776.93	5.218	0.712	−0.130	1.0	0.9	55.3	H
7786.51	5.169	0.709	−0.129	0.0	−1.5	122.1	S H
7802.47	5.089	0.704	−0.127	1.7	1.9	222.8	S H
7821.79	4.993	0.697	−0.124	−1.5	−3.0	355.1	MH
7831.49	4.945	0.693	−0.123	−0.8	0.5	64.5	S H
7844.38	4.880	0.688	−0.121	2.5	0.2	159.8	S
8229.49	2.993	0.388	−0.039	2.0	−1.7	308.0	S
8242.14	2.932	0.363	−0.035	0.0	−0.7	36.0	M
8278.29	2.757	0.286	−0.026	−0.1	1.5	250.0	S H
8290.83	2.697	0.261	−0.023	1.2	1.1	333.4	S H
8327.41	2.523	0.200	−0.013	0.3	−0.5	209.4	S H
8339.38	2.462	0.183	−0.010	−0.2	1.7	295.8	S H
8375.91	2.292	0.137	−0.001	−1.4	0.0	185.5	S H
8388.46	2.232	0.122	0.003	0.0	−0.5	256.3	M
8424.26	2.065	0.087	0.013	1.1	0.8	117.6	S H
8436.78	2.005	0.076	0.017	2.7	−0.8	205.2	S H
8474.16	1.828	0.042	0.028	2.2	−0.7	100.4	S H
8486.66	1.770	0.033	0.031	1.1	−1.4	182.2	M
8523.05	1.600	0.012	0.042	−2.2	−2.2	82.5	S H
8535.24	1.543	0.006	0.046	−1.4	−2.5	170.8	S H
8572.36	1.372	−0.010	0.057	−1.7	0.0	54.6	S H
8584.89	1.313	−0.016	0.061	1.3	1.4	132.1	S H
8621.05	1.143	−0.032	0.072	1.2	−0.8	32.3	S H
8633.58	1.084	−0.039	0.075	0.2	0.3	121.2	S H
8670.88	0.911	−0.050	0.080	−1.0	−0.4	355.1	S H
8683.40	0.852	−0.053	0.079	0.5	0.2	76.3	M
8719.03	0.686	−0.056	0.070	0.3	−1.1	303.9	S H
8731.55	0.629	−0.054	0.065	2.6	−1.0	26.2	S H
8769.42	0.455	−0.044	0.044	−0.2	−0.9	274.4	S H
8782.15	0.397	−0.038	0.038	−0.2	−0.2	8.0	S H
8810.58	0.269	−0.017	0.028	−1.1	−0.7	194.9	H
8813.58	0.255	−0.014	0.028	0.7	−0.3	213.4	H
8817.61	0.237	−0.011	0.026	1.0	0.9	237.9	H
8822.48	0.215	−0.009	0.025	1.6	−0.7	267.3	H
9008.50	48 cm	0.000	0.000	−3.1	0.8	193.0	SMH

Note: MT, mission time; Altit, altitude in km; *X*, zonal position in km (longitude east = 167.661° + *X*/44.22); *Y*, meridional position in km (latitude = −10.251° + *Y*/44.94); Pitch and Roll in degrees; Azim, azimuth of DISR (Huygens *z*-axis) east of north in degrees; SMH, listed whenever a SLI/MRI/HRI image was received.

magnitude. The elevation encoder seemed to be as accurate as required, and a backlash in elevation would not be expected since the weight of the camera was not perfectly balanced. Since we had 30 measurements, far more than the three required to determine the six constants, we could check the distortion measurements of the first method. It turned out to be accurate to 0.02°. From the fit of all data, we estimate that we know the relative azimuth and elevation angle for each pixel to 0.03° accuracy.

There is a small overlap between the fields of view of the SLI and MRI and a larger overlap for the MRI and HRI. When we aligned features visible in descent images in those areas, we found that the apparent orientation between the imagers must have shifted by 0.1° since our laboratory measurements, probably caused by a relative shift of about 0.02 mm between optical components. We adjusted the geometry accordingly. This shift could have happened at one specific time, or it could be due to temperature, since the temperature of the optics was much colder when surface features were visible than the room-temperature laboratory.

2.3. Deconvolution of the point spread function

Quantitative analysis of the contrast of small features seen in the images requires the knowledge of the point spread function (PSF). Sub-sampled PSFs of the three imagers were measured in the laboratory by taking 16 images of a point source and moving the camera by each combination of quarter pixels in the horizontal and vertical direction between images. For each imager, this procedure was repeated at least six times at different areas of the field of view in order to record the spatial variation of the PSF.

The observed PSFs varied too much with location in the field of view in order to predict the PSF for a specified

location. On the other hand, they were similar to ray-trace plots calculated from the design of the lenses. Therefore, we used the following model to describe the PSF for any specified location.

For each imager, we adjusted 13 free parameters in order to fit all observed PSFs. Our solution is based on a least-squares fit. The 13 parameters are: the coma (2 parameters), astigmatism (1), defocus (2), angle of the focal plane (2), spherical aberration (2), the location of the optical axis (2), and two parameters for the location of the obstruction (small mirrors reflecting the light of a calibration source during calibration cycles). With these 13 parameters for each imager, we generated about 2000 PSFs across the fields of view, one PSF for each 8×8 pixel square.

We deconvolved each image by using the Wiener method combined with a final PSF of Gaussian shape with 1.0–1.5 pixels full-width-half-maximum. For each section of the image, we used the PSF for the four closest of the 2000 locations. We then interpolated between these four results with a weighting decreasing with the distance between the location and the location for the PSF. This method provided smooth transitions between neighboring image sections. For two of the three imagers, the HRI and SLI, deconvolution caused only a minor improvement. For the remaining imager, the MRI, however, the deconvolution changed the images significantly, because it had PSFs consisting of a brighter core with a radial tail of up to 6 pixels long. In the original images many features seem to consist of radial streaks, which are not present in the deconvolved images, showing that they are artifacts of the elongated PSF.

2.4. Intensity calibration of the imagers

In the laboratory, the sensitivity of each imager was measured by imaging of a monochromatic light source every 10 nm of wavelength across the whole region of spectral sensitivity (600–1100 nm). The sensitivity is near the maximum between 670 and 800 nm and close to zero below 640 and above 920 nm, and the mean wavelength is about 775 nm. Furthermore, flatfields were taken in an integrating sphere of known intensity at seven different temperatures of the CCD. For each imager, the sensitivity decreased with decreasing temperature. Since the decrease was linear within 0.3%, we adopted the least-squares linear fit to define the sensitivity as function of temperature. This function was used to convert all data numbers into intensity. Furthermore, these values were converted into reflectivities I/F, where I is the measured intensity and πF is the solar flux at the top of Titan's atmosphere, which is about $15\,W/m^2$ for the probed spectral region.

Because the mean wavelength for the three imagers is slightly different by up to 3 nm, one would not expect perfect agreement in the recorded I/F of simultaneous, spatially overlapping images. Indeed, the differences are up to $\pm 1\%$. Because these differences seemed to slowly drift during the descent due to the increasing strengths of methane absorptions, we applied a small calibration correction to the MRI and HRI images so that overlapping areas match very well. This means that we effectively changed the mean wavelength of both imagers to that of the SLI.

2.5. Data compression of images

The communication link between Huygens and Cassini allowed the transmission of a few megabytes of data during the descent. This is several times less than what would be needed to transmit most of the information visible to the DISR imagers without data compression. Since many images taken during the descent had little contrast and information, even somewhat less than expected, they could be compressed by a large factor without significant loss of information.

The images with 12 bit/pixel were compressed to 1 bit/pixel through a two-step process. In the first step, 12-bit data numbers were mapped to 8-bit numbers via an adaptive scheme. For each image, the range of data numbers was determined, excluding a few pixels on each end of the distribution accounting for possible bad pixels such as cosmic ray hits. Within this range the mapping was up to 10 times finer than without the adaptive scheme. Outside this range, the mapping was up to twice as coarse as without the adaptive scheme. Furthermore, the mapping was finer at small data numbers accounting for the random photon noise, which is proportional to the square-root of the data number. This mapping preserved all information for the MRI and HRI images. On the other hand, most SLI images suffered a slight degradation due to quantization noise in this step because of their wide range of data numbers, ranging from the typically dark surface looking down to the bright sky looking above the horizon. The wide range prevented the use of the adaptive scheme for many SLI images.

The second compression step used a hardware compressor to reduce 8-bit images in 16×16 pixel blocks to about 1 bit/pixel on average. It used the discrete cosine transform with further quantization, truncation and a special coding scheme to arrive at the final compression factor. For most images, the degradation done by compression was less than that due to CCD noise. However, for a few images with many features, the image quality was somewhat degraded.

While the difference between uncompressed and compressed images is typically less than the photon noise, the compressed images are difficult to interpret without further processing. For example, in areas with no significant features, the uncompressed images show only photon noise, and its interpretation is unambiguous. On the other hand, the compressed images show periodic patterns indicating the few strongest spatial frequencies in the noise which made it through the compressor. The periodic patterns are different in each 16×16 pixel block. They are eye catching and distract from subtle but real features

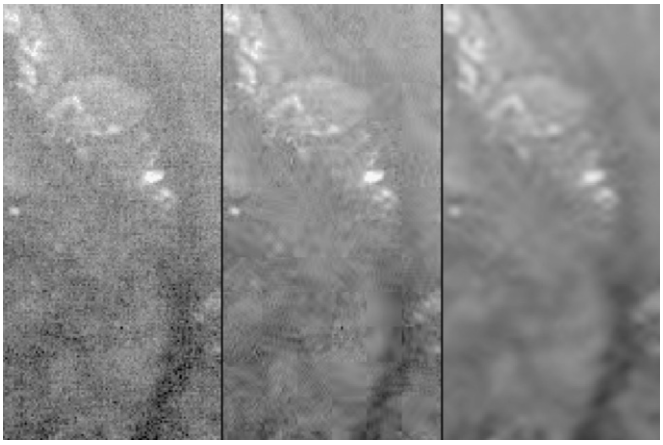

Fig. 1. A 200-m wide section of image # 696, taken from 1.1 km altitude, in three versions. The central part is the image as transmitted. The left part has simulated CCD photon noise added where the decompression algorithm truncated data. The right part has the CCD photon noise smoothed so that only real surface features remain visible. The display is strongly contrast enhanced since the contrast between the darkest and brightest feature in this image is only 3%.

on typically larger scales. Therefore, in the Fourier transformed domain, we reduced amplitudes whenever they were similar or smaller than the photon noise level. The reduction factor was selected to be dependent on the compression factor in each 16×16 pixel block, since blocks with a large compression factor required larger reduction factors than blocks with many transmitted features. This smoothing operation eliminated all features below the noise level. Therefore, all features remaining visible are likely to be real, which facilitated further image analysis (cf. Fig. 1).

2.6. Flatfielding

Simple flatfielding consisted of the division of each image by the flatfield taken in the integrating sphere. We improved this by two observations. First, the intensity in the integration sphere was measured to have variations of typically 1% in intensity, although in one corner of the HRI up to 5%. Second, several small-scale features of about 1% in intensity consistently appeared in images taken above 100 km altitude. Since surface features were of very low contrast at 50 km altitude, since there is significant haze between 50 and 100 km altitude, and since the features appear stationary in the images, they must be flatfield features. Therefore, we used the images taken above 100 km altitude to improve the flatfielding on small scales.

On very small scales, the flatfields have a lot of structure due to transmission variations of the fiber optics. In order for the image compression to work effectively, we flatfielded the raw images on-board before sending them to the compressor. In the laboratory, we noted that the structure of the flatfields shifts by 0.2 pixel between the coldest and warmest measured temperatures, probably due to a slight shift of the fiber optics conduit with respect to the CCD. In the descent images, we also noted a shift of flatfields with temperature, because the strongest flatfield features were not completely taken out by the constant on-board flatfields. From these remaining features, we estimated that the shift of flatfields with temperature was only about half as much as in the laboratory, and in a slightly different direction. The different behavior was probably due to a different temperature distribution within the instrument in Titan's atmosphere compared to the laboratory. Using the amount of shift and its direction during the descent, we applied the appropriate flatfield correction to each image.

2.7. Dark current

The dark current as function of temperature was monitored multiple times during the seven-year cruise to Titan. For each pixel, the dark current was increasing from year to year, but the pixel-to-pixel structure remained relatively constant. For the images at Titan, we used the structure of the dark current from the latest checkout and scaled it according to counts in dark images taken during the descent. We subtracted the dark current counts from the recorded counts.

2.8. Recorded light during readout

The CCD had no shutter. At the end of each exposure, the accumulated charge was transferred to the other half of the chip along columns at a speed of 2 μs per row. We accounted for the accumulated charge during the transfer row by row. The last row had no such problem. Therefore the row before the last row can be corrected by subtracting the counts of the last row scaled by the ratio of 2 μs to the exposure time. Then the previous row can be corrected, and so on.

2.9. Smeared images

Three of the 600 images show an obvious smear. A few further images may be smeared too. We measured the smear angles and concluded that the angular speed of Huygens was near 8°/s for the three images. We estimated upper limits of the angular speed for other images based on image scale and the sharpness of features in the image. We concluded that typical rms angular speeds of Huygens were near 5°/s in the lower 10 km. Upper limits for rms values are 10°/s between 10 and 20 km altitude and 15°/s between 20 and 30 km altitude. All these estimates are for HRI images, where the component of the rotational angular speed was only 2–3°/s. Thus, a large part of the angular speed of Huygens was not due to rotation but due to swing, at least during the final part of the descent, when the rotation was slow.

3. The surface mosaic

With all images calibrated, we now can start to create a mosaic of the surface features by putting together 236 descent images containing significant surface detail. Once the position and orientation of Huygens is known at the time of each exposure, we can project each image onto Titan's surface, which is assumed here to be a perfect sphere of radius 2575 km. Images taken below 30 km altitude have typically enough features so that the puzzle can be put together without a priori knowledge of position or orientation. Images taken between 30 and 50 km altitude can usually be added to a mosaic made from images at lower altitudes. Images taken above 50 km altitude do not have enough features to make a valuable addition to the mosaic. In order to achieve an accurate mosaic, we used the following method to constrain the position and orientation of Huygens at each exposure.

We start with the assumption of zero pitch and roll, but adjust the remaining three parameters (longitude, latitude, and azimuth) for each exposure. Note that the altitude was fixed before. One can create a mosaic with all images roughly fitting. However, the trajectory for this fit is not smooth at all, but more like a zigzag. A better estimate for the trajectory is then determined by averaging positions within a cycle (about 2 min). In order to fit the features with this trajectory, one needs to allow non-zero pitch and roll angles. The fit becomes better than the original one. Some image pairs, however, will only fit together with a different trajectory. Therefore, the trajectory gets adjusted, which then changes pitch and roll angle, which then improves the fit. After several iterations, the solution converges and most images fit to the mosaic as accurately as features can be located, typically to somewhat better than one pixel. This iteration required a significant part of the total effort for this work, because there are some 830 free parameters (five parameters for 166 exposures) which needed to be adjusted manually for each iteration. During this process, we took care that the constraints about average pitch and roll described in Section 4 were incorporated in the solution.

The last 20 SLI images, starting at 3.0 km altitude, show the horizon. Based on the assumption of a flat, spherical surface, we determined for each of these images the pitch and roll. Pitch angles were accurate to 0.2°, roll angles accurate to 1°. Considering that typical elevation differences are on the order of 100 m according to radar data (Svedhem, private communication), these angles may be biased by 0.1° or 0.2° due to topography, which is less than the measurement accuracy. Based on measurements of the vertical intensity gradient near the horizon and comparison with models, we estimated that the total optical depth of the atmosphere is 0.05/km for the lowest 3 km of altitude. This compares well with Tomasko et al. (private communication), reporting a haze optical depth of 0.03/km, methane absorption of 0.01/km, and Rayleigh extinction of 0.005/km near the surface for the spectral passband of the imagers.

Constraints on the Huygens speed come independently through the Doppler Wind Experiment (DWE) by Bird et al. (2005). The Doppler shift measurements constrain the component of the Huygens speed towards Earth during 42 sections of the descent with linear interpolation assumed for the intermediate sections. Forty gaps were due to calibration requirements while one longer gap was during the switch from one radio telescope to another one on a different continent. We found that our constraints on the trajectory are consistent with DWE results for all 42 sections and for 39 of the 41 gaps. Thus, we adopted their data for all these sections, but modified their linear interpolation during the long gap, between 12 and 5 km altitude, and during one of the short gaps, near 2 km altitude, where our constraints are inconsistent with linear interpolation. Because our accuracy of the determination of the trajectory is about 1% of the altitude, while Bird's accuracy is almost independent of altitude, our contribution to the zonal motion is restricted to lower altitudes.

For the motion perpendicular to the direction of Earth, we selected the smoothest trajectory consistent with our data. In order to constrain the rotation of the mosaic, we used additional data discussed in Section 5. In order to constrain the position of the mosaic with respect to Titan's latitude and longitude grid, we used the Cassini radar image as discussed in Section 6.

Our trajectory is well constrained below 30 km altitude and weakly constrained between 30 and 50 km. Above 50 km altitude, no information on trajectory could be inferred from DISR data since surface features were not clearly visible through more than 50 km of haze. However, the parachute deployment location near 150 km altitude is known quite well (Kazeminejad et al., 2007). The location estimated from DISR data at 50 km altitude is in the direction of 88° azimuth (2° north of east) from the DTWG location near 150 km, and the distance between both locations is in good agreement with DWE constraints (Bird et al., 2005). We therefore extended our trajectory from below 50 up to 150 km altitude by a smooth curve fitting the coordinates at parachute deployment.

For the purpose of obtaining the geometry and matching features, it is not necessary to match image pairs photometrically, yet it greatly facilitates if images can be combined into a large mosaic without large photometric jumps at the image edges. After accounting for the brightness of the atmosphere between the camera and the surface, both for the transmission of the atmosphere and its intensity contribution (cf. Section 4), images of the same feature still did not match well in intensity. This is significantly improved by applying a photometric function to the image brightness: $I/F \sim \{0.985 + 0.015(\cos\alpha + 0.55)^6\}/(0.85 + 0.15\cos\beta)$, where α is the phase angle and β the nadir angle. Considering that the illumination near the surface was about 10% direct sunlight and 90% diffuse light concentrated toward the Sun, the first term implies a

moderately backscattering surface, while the second term indicates a somewhat rough surface. For the purpose of mosaicing, the physical meaning of the photometric function was not important. A separate study in progress will use the photometric variations to infer optical properties of the surface.

In order to obtain a mosaic with almost invisible image edges and low noise, we used all images with a strong weighting toward images with the best pixel scale. The weighting was proportional to the fourth power of the pixel scale in the vertical direction with a further weighting to favor images from lower altitudes due to the feature contrast improving toward lower altitudes. This method was satisfactory away from image edges. At many edges, however, a slight mismatch of the general intensity was detectable, especially at the edges of high-altitude images. This is understandable considering that the contribution of light from the haze was some 100 times as large as the difference between bright and dark features at higher altitudes (30–50 km). Thus, an estimation of the haze brightness off by less than 1% for one particular image would cause a significant brightening or darkening in the mosaic inside the area of the image, causing the edge of the image to be apparent.

In order to achieve smooth transitions at all image edges, we added a further step. We required that the difference in reflectivities between neighbor pixels (horizontal and vertical) should be as close as possible to the average recorded differences. This method required a lengthy iteration, but it eliminated discontinuities in intensity at image edges.

We combined all image data into a mosaic. Because the image scale changed by five orders of magnitude between images taken at 50 km altitude and those taken at 48 cm altitude, a mosaic of Titan at a pixel scale fine enough to show the finest detail would require millions of pixels for each axis. Instead we chose a projection similar to a moderately sized Mercator projection to map all images at sufficient scale (Fig. 2). Note that near the landing site, corresponding to the lower half in Fig. 2, some areas were imaged at much higher resolution than other, nearby areas. In order to facilitate interpretation of the mosaic, we color-coded each location according to the resolution in the image with the best image scale. The color bar is shown in Fig. 3.

Near the landing site, where the color in the mosaic varies between red and blue, the resolution varies by two orders of magnitudes. In some areas, overlap between adjacent images was not sufficient to accurately place individual images. Further away from the landing site, between 500 m and 5 km from the landing site, the consistently blue–green color indicates good coverage. Indeed, in this region, the mosaic should be quite accurate allowing quantitative measurements. Further away from the landing site, in the blue and purple region, especially further away than 10 km, the coverage was inferior again, with many regions only covered by single images. In this area, features may be represented with significant distortion, orientations of features could be off by several degrees, and actual sizes could be easily 5% larger or smaller than according to the mosaic.

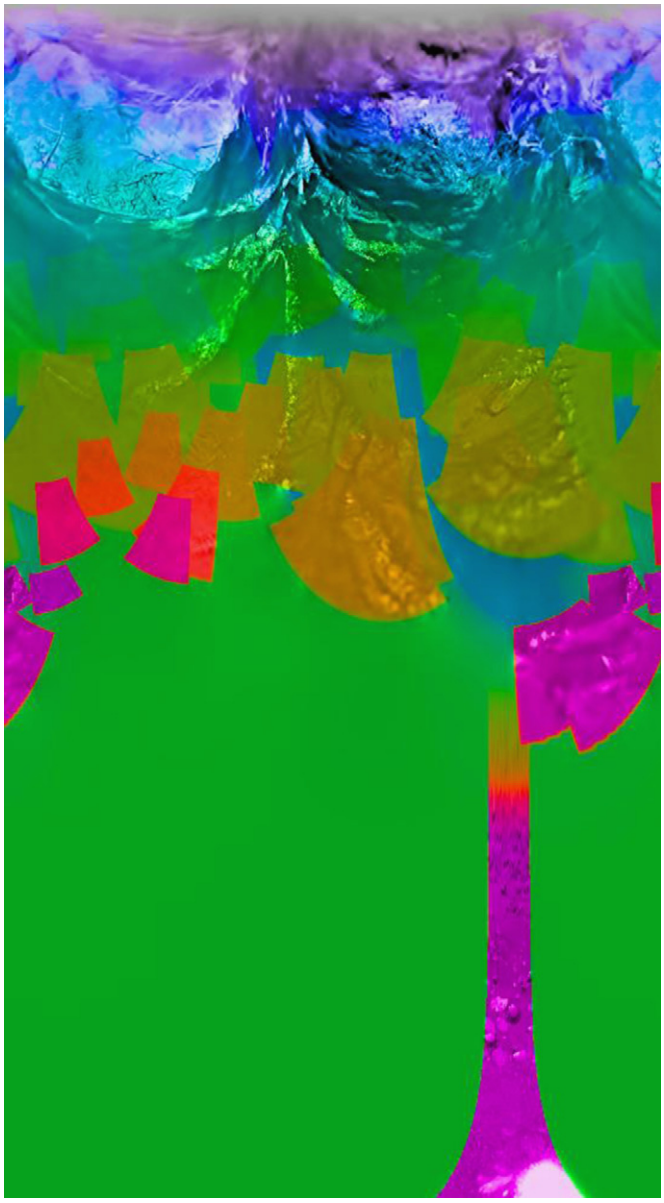

Fig. 2. A Mercator projection of the surface mosaic as seen from 20 km above the landing site. At each place, the color is coded according to the resolution in the best-resolution image (cf. Fig. 3). It is centered on east, while west is very close to the left and right edge, due to slight overlap. The vertical extent is from a nadir angle of 90° (top) to a nadir angle of 1 arcsecond (bottom), which corresponds to a radius of 10 cm around the sub-DISR point after landing.

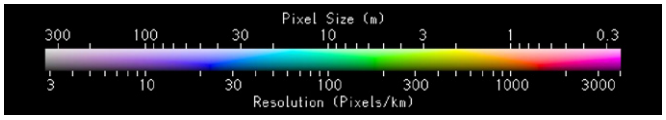

Fig. 3. The color coding for Fig. 2. The top and bottom of the color bar shows the color coding for bright and dark areas, respectively. Areas with a resolution better than 25 cm per pixel are coded in the same color.

4. The sky mosaic

Our SLI images reach up to 6° above the horizontal direction on average. Near the surface, this gives only 6° of sky coverage. However, at an altitude of 30 km, the horizon is 9° below the horizontal direction. At the beginning of the DISR measurements, at 145 km altitude, this value is 19°, leaving about 25° of sky coverage. At the highest altitudes, even below the horizon most of the light comes from the atmosphere, not from the surface.

We analyzed the sky in the 124 SLI images before landing, the 87 SLI images after landing, and the 101 SLI strip images, taken above 30 km altitude. The SLI strip images have the full vertical resolution, but contain only two resolution elements in the horizontal direction, near the left and right edge of the SLI field of view, which still yields most of the useful information about the sky brightness distribution. In each row of 128 pixels, only the averages of columns 7–19 and 110–122 are transmitted.

We found that the sky brightness can be very accurately approximated by a function of altitude, zenith angle, and phase angle, which means that intensities in directions symmetrical to the Sun and nadir are identical. Image pairs taken at similar altitudes and at similar angles to the left and the right of the Sun were mirror images to better than 1% intensity when allowing for a shift and rotation, although the intensity variation across each image may have been more than 50%. If the haze had slightly different properties to the north versus the south of the trajectory, these image pairs would not have been such a perfect match. Since the path between successive scatterings of a photon in the haze is on the order of 20 km at the wavelengths probed, one may not expect a significant variation of the haze properties over the relatively small area probed. Near the surface, however, we found features of about 1% in amplitude in the sky brightness which are not symmetrical to the Sun. A comparison with surface albedo maps shows that the sky brightness is correlated with the surface albedo in the distance in the general viewing direction. Clearly, this asymmetry is due to illumination of the atmosphere from the surface.

We tried to put together the sky images to create a sky mosaic. One purpose for such a mosaic is that accurate knowledge of the sky brightness distribution at different altitudes gives tight constraints on the vertical distribution and on the shape of the phase function of aerosols. In this work, however, we will use the mosaic only to infer the orientation of Huygens for each exposure.

Because the sky brightness decreases rapidly toward lower altitudes, only images taken at similar altitudes can be combined into a mosaic. We divided the descent in typically 5–10 altitude ranges for this purpose. At first, we assume zero pitch and roll angle and use the azimuth angle determined in Section 5. This yields sky mosaics for a few altitudes. From neighboring mosaics, one can measure the gradient of sky brightness with altitude at each combination of nadir angle and phase angle. With this gradient, one can correct the brightness for images of different altitudes within each mosaic. With this correction, images fit better together. Then, we improved the fit by allowing for non-zero pitch and roll angles. The improved mosaics allow more accurate determinations of the gradient with altitude. Similar to the creation of surface mosaics, this method required several iterations.

When allowing the pitch and roll angles for each exposure to float, there is one parameter, which cannot be determined by this method, which is the average tilt of Huygens towards or away from the Sun. Such a tilt would rotate the mosaic in such a way that contours move up below the Sun and down opposite to the Sun or vice versa. In order to fix this single parameter for each mosaic, we used the DWE zonal wind speeds by Bird et al. (2005) in the following way.

We differentiated DWE data in time which gives the horizontal acceleration of Huygens toward the azimuth of the Earth (note that the Earth was within 0.1° of the Sun, because it transited the Sun as seen from Titan just a few hours earlier). Because the parachute is larger than Huygens and carries much less mass than Huygens, each acceleration of Huygens must be due to a tilting of the parachute toward or away from the Sun, except for short-period swinging of the parachute lines. Thus, the tangent of the Huygens tilt on average is the ratio between the acceleration of Huygens and Titan's gravity at that altitude. Our data also indicate that this relation is true as discussed in Section 10.3. Therefore, the acceleration from DWE data yields the average zonal tilt of the Huygens–parachute axis with respect to the vertical. This tilt is listed in Table 2 with positive values indicating that the parachute was further east than Huygens. Meridional tilt components cannot be inferred through the DWE data. Also, the tabulated tilts do not include the high-frequency component discussed in Section 7. Since Table 2 is mostly based on DWE data, which has many gaps of more than a minute, the tilt values relevant to these gaps and listed in Table 2 are based on linear interpolation between measured data.

We created sky mosaics for 5–10 altitude ranges. The mosaic for the highest altitude is shown in Fig. 4. Each mosaic has some azimuths with missing data. In order to achieve our goal of knowing the sky brightness for every combination of altitude, zenith angle, and azimuth, we could have done some sophisticated three-dimensional interpolation based on the mosaics. However, we decided to create an analytical function, which gives the brightness as function of altitude, zenith angle, and azimuth. First, we fitted the function to the mosaics. Later, we fitted the function directly to each image. The final function had 19 adjusted parameters and fitted the data to 2% rms and is given in Appendix B. Since this is a smooth function, it cannot deal with small-scale features in the sky brightness. However, the only small-scale feature we could find was the thin haze layer at 21 km, described by Tomasko et al. (2005), clearly visible in three images taken from 21 km

Table 2
East–west tilt function of Huygens, low-frequency component

MT (MT+)	0	6	12	18	24	30	36	42	48	54	60	66	72	78	84	90	96	102	108	114
0	31.5	30.9	30.1	29.2	28.0	26.6	24.7	22.7	20.4	18.1	15.9	14.1	12.4	10.9	9.6	8.4	7.2	6.0	4.8	3.6
120	2.4	4.0	4.5	8.6	5.5	1.6	4.4	8.2	5.3	−1.4	−3.6	−3.5	5.1	1.9	3.3	−6.0	−3.2	−2.5	−2.7	−1.2
240	1.0	3.2	5.4	7.7	8.7	6.5	4.4	2.3	0.2	−1.7	−3.6	4.2	1.6	−4.8	−4.8	1.3	2.2	−5.7	0.6	3.7
360	−3.7	−14.8	−10.5	−0.8	−0.8	−9.2	−8.7	8.0	7.7	7.4	7.1	6.8	6.6	3.4	−0.5	−4.3	5.3	−0.1	−9.8	−5.7
480	2.2	−3.8	−2.0	6.3	0.8	7.5	9.0	4.4	0.1	−3.2	−0.4	−0.7	2.4	5.1	6.0	2.2	5.2	4.9	4.7	4.4
600	4.1	3.5	2.1	0.6	−0.8	−2.3	−3.7	−5.2	−6.6	−8.0	−9.5	−15.1	−11.2	−5.4	−5.7	−5.7	−3.2	−5.0	−10.3	−12.8
720	−8.5	−0.4	−2.2	1.9	−0.4	−10.8	−12.3	−10.1	−8.0	−5.8	−3.6	−2.2	−3.6	−5.1	−6.5	−7.9	−9.3	−10.8	−12.2	−4.6
840	−1.1	−11.8	−2.3	−5.2	−12.3	−10.5	−0.8	−1.5	−2.8	−4.1	−5.4	−6.7	−8.0	−9.2	−8.2	0.0	−4.3	3.3	4.2	5.2
960	6.1	−0.5	−9.4	−4.2	−5.7	−7.0	−5.5	−4.0	−2.6	−1.1	0.4	−1.0	4.3	1.1	1.5	−2.4	−1.0	−3.8	−4.5	−1.5
1080	−2.2	−4.4	−3.6	−2.3	−0.8	−5.8	−5.9	−5.5	−5.1	−4.8	−4.4	−4.1	−4.3	−4.6	−4.8	−4.9	−4.0	−3.2	−2.4	−1.5
1200	−0.7	−5.8	−3.2	−7.7	−5.1	−7.0	−7.7	−5.6	−7.4	−5.7	−8.9	−10.6	−10.6	−6.7	−4.2	−7.7	−7.7	−6.5	−6.5	−6.4
1320	−6.3	−6.2	−6.2	−4.4	−3.3	−2.9	−2.4	−1.9	−1.4	−0.9	−0.4	−0.3	−8.0	−7.4	−3.6	−1.7	−2.7	−3.2	−3.2	−5.1
1440	−6.7	−6.6	−8.3	−5.4	−4.0	−5.0	−3.0	−1.3	−1.2	−1.1	−1.0	−0.9	−0.8	−0.7	−0.6	−0.6	−1.0	−2.0	−3.2	4.1
1560	0.8	2.5	0.1	2.1	−0.7	−0.5	1.1	−2.1	3.4	4.1	8.0	8.8	10.4	10.2	11.2	8.3	5.2	6.0	6.8	7.5
1680	8.3	9.1	9.8	10.6	11.3	12.1	12.9	10.9	7.2	3.5	5.4	6.5	4.6	2.6	2.9	0.1	−0.9	1.2	−1.0	0.6
1800	−0.6	0.0	0.3	0.1	−1.0	1.3	2.8	2.8	2.7	2.6	2.4	2.3	2.2	2.0	1.9	1.8	1.6	1.5	1.4	1.2
1920	1.1	4.3	0.4	1.1	0.0	0.2	0.4	1.4	−1.2	0.4	0.6	−0.6	−1.0	−0.6	1.6	2.8	−0.7	−1.2	−1.2	−1.2
2040	−1.2	−1.1	−0.7	−0.3	0.0	0.4	0.8	1.1	1.5	1.9	0.1	1.8	−1.8	−1.1	−3.4	−1.6	1.7	−2.4	−2.3	−0.4
2160	−1.2	−2.3	2.6	−0.3	−1.7	−0.8	−0.8	−2.4	−4.0	−4.3	−4.1	−3.7	−3.4	−3.0	−2.7	−2.3	−1.9	−1.6	−1.5	−1.8
2280	−2.0	−1.9	−1.5	−2.0	−1.4	−0.6	0.7	−0.3	−2.4	−1.2	−1.5	0.0	−2.2	−1.2	−0.8	−1.2	−0.9	−0.7	−0.4	−0.1
2400	0.2	0.5	0.8	−2.4	−5.0	−3.5	−2.1	−0.6	−0.2	0.0	0.3	0.4	0.1	0.2	1.4	−2.0	−1.5	−0.9	−1.1	−1.6
2520	−0.8	−0.8	−0.9	0.6	1.4	0.6	−0.3	−0.5	−0.5	−0.4	−0.2	−0.1	0.0	0.2	0.3	0.4	−0.6	−1.7	−2.2	−2.1
2640	−2.0	0.9	−2.5	−1.6	0.4	0.6	−0.8	−0.7	0.8	−1.6	0.9	−1.6	−1.4	0.3	−0.3	0.5	−1.7	−3.6	−3.5	−3.5
2760	−3.4	−3.4	−3.3	−3.3	−3.2	−3.2	−3.1	−2.2	−1.0	0.3	1.5	1.4	−1.6	−2.3	−2.0	−1.7	−0.3	−0.3	−0.3	0.8
2880	−1.6	−0.3	−0.9	−1.3	−0.1	2.3	−3.8	−0.8	1.8	1.8	1.8	1.8	1.8	1.8	1.8	1.8	4.8	5.5	4.1	2.8
3000	1.4	0.0	−1.8	0.5	−0.6	−0.8	−4.8	1.8	1.7	−5.4	−5.1	1.1	−2.8	0.4	0.2	0.2	4.8	3.9	3.0	2.1
3120	−2.4	−4.1	−1.1	0.3	0.3	0.3	0.2	0.2	0.2	0.2	0.2	0.7	0.1	−1.3	−3.6	−1.5	−1.3	−2.8	0.6	−0.9
3240	−0.2	1.0	0.3	1.6	0.5	−1.4	−0.7	1.4	3.5	5.3	−2.7	−4.1	−0.6	2.3	2.3	2.3	2.3	2.2	2.2	2.2
3360	2.2	2.5	0.2	−1.1	−0.7	−1.0	−1.7	−0.1	0.2	−0.9	−0.5	0.5	1.4	−1.6	1.2	−0.5	1.3	1.7	2.2	2.5
3480	−0.2	−0.8	0.9	2.2	1.7	1.1	0.6	0.0	−0.5	−1.1	−1.6	−1.3	0.6	0.0	−0.9	−0.2	−1.5	1.5	0.2	0.2
3600	−0.7	0.1	0.1	−0.3	0.0	0.8	1.1	0.5	0.3	0.1	−0.8	−0.1	0.7	1.4	−0.7	0.7	3.6	2.1	0.0	−3.0
3720	−6.0	−0.3	0.2	0.2	0.2	0.4	0.9	0.7	−1.6	2.4	−1.9	−0.6	−2.5	0.8	0.7	0.0	−0.6	−8.5	−7.7	−6.7
3840	−5.7	−4.7	−3.6	−2.6	−1.6	−0.6	0.4	1.4	2.4	0.6	−0.6	2.5	2.2	1.8	1.3	0.8	0.4	−0.1	−0.6	−0.2
3960	0.2	−0.8	0.1	−1.3	−0.7	−0.3	0.9	2.1	1.2	0.3	−0.6	−1.5	−2.4	−3.3	−4.2	−5.1	−6.0	−6.9	−5.5	−2.5
4080	−1.6	−1.5	0.0	0.2	−1.3	−1.6	0.4	0.9	0.8	−0.4	−0.9	−0.2	0.3	1.1	0.0	−3.3	−4.2	−5.0	−4.6	−4.3
4200	−4.0	−3.6	−3.3	−2.9	−2.6	−2.2	−1.9	−1.6	−1.5	−3.3	−3.2	−0.4	−0.4	−0.5	−0.8	−1.4	0.5	2.9	0.3	−1.5
4320	−1.3	−0.3	−0.5	−1.9	−0.8	1.1	−0.1	−1.4	0.8	3.8	2.3	1.2	0.4	0.0	1.4	2.4	3.4	4.5	0.3	−0.7
4440	−0.9	−2.2	0.6	−0.1	1.4	−0.5	0.1	0.1	−0.4	−0.8	1.3	0.9	0.6	2.1	−3.1	−2.2	−3.0	−2.9	−2.7	−2.6
4560	−2.5	−2.3	−2.2	−2.1	−1.9	−1.8	−1.7	−1.5	−1.4	−1.3	−1.1	0.3	−0.9	0.8	0.2	−0.2	−1.3	−0.8	0.4	1.0
4680	−0.4	−0.6	−0.2	1.4	−0.5	1.9	1.7	1.5	1.2	1.0	0.8	0.6	0.4	0.1	−0.1	−0.3	−0.5	−0.8	−1.0	−1.2
4800	−1.4	−1.8	1.5	−0.4	−0.8	−0.8	−0.5	0.1	−0.9	−1.6	−1.5	1.1	−0.8	0.3	−0.9	0.0	−1.2	1.9	1.2	0.2
4920	0.6	0.9	1.3	−0.3	0.0	1.4	0.6	−0.1	−0.9	−1.6	−0.7	1.2	−1.5	−2.2	0.0	0.8	0.2	−1.6	−0.2	1.2
5040	−0.4	−1.4	−0.5	0.1	0.2	0.2	0.2	0.2	0.2	0.2	0.2	0.1	0.1	0.1	0.1	0.1	0.1	0.1	0.1	0.1
5160	0.0	0.0	0.0	−0.8	−0.9	1.0	1.0	0.5	−0.9	−1.0	−0.6	−0.7	0.7	−0.5	−1.5	1.3	1.4	0.5	0.9	1.5
5280	2.2	−0.9	−1.8	1.0	2.2	1.8	1.3	0.8	0.3	0.7	1.2	1.6	2.1	−0.6	0.2	0.3	0.3	0.2	0.2	0.8
5400	0.5	−1.0	1.0	−1.4	−0.2	−0.3	−0.4	−0.3	−0.3	−0.2	−0.2	−0.1	−0.1	0.0	0.0	0.1	0.1	0.2	0.2	0.3
5520	0.3	1.1	0.8	−0.6	−1.1	3.8	−0.2	−0.4	0.2	0.4	0.3	−0.6	−1.0	−0.3	1.1	3.2	2.4	2.2	2.1	2.0

Table 2 (*continued*)

MT (MT+)	0	6	12	18	24	30	36	42	48	54	60	66	72	78	84	90	96	102	108	114
5640	1.8	1.7	1.6	1.4	1.3	1.2	1.0	0.9	0.8	0.6	0.5	0.3	0.2	−0.1	−0.6	−0.2	1.9	−1.4	−0.2	0.6
5760	−0.3	0.4	0.8	−0.1	0.2	1.2	0.8	0.2	−1.3	−1.4	−1.4	−1.3	−1.3	−1.2	−1.1	−0.9	−0.8	−0.5	−0.3	−0.1
5880	−0.5	−1.1	−0.4	−0.6	−0.7	0.1	0.3	−0.1	−0.7	−0.5	−1.3	−0.9	−0.6	−0.3	−0.2	−0.2	−0.3	−0.2	−0.2	−0.1
6000	−0.1	0.0	0.0	0.1	0.2	0.2	0.3	0.3	0.4	0.4	0.5	0.6	0.1	−0.4	−0.6	−0.5	0.2	−2.8	−0.1	−1.0
6120	−1.9	−0.6	0.8	0.8	1.1	0.8	−0.7	−0.3	0.1	0.4	0.8	1.1	1.5	1.8	2.0	1.8	0.8	−0.3	−0.4	−0.3
6240	−0.1	0.1	0.3	0.3	0.1	−0.1	−0.1	0.1	0.2	0.2	0.2	0.0	0.0	0.1	−0.5	−0.3	−0.1	0.2	0.4	0.6
6360	0.8	1.1	1.3	1.5	1.7	2.0	2.2	2.4	2.1	−1.8	−0.9	0.4	0.3	0.2	0.1	1.1	−0.8	−3.0	−1.6	−0.3
6480	0.9	2.0	1.6	1.1	1.3	1.5	1.7	1.9	0.0	−3.8	−2.9	−2.0	−1.0	−0.1	0.8	1.7	1.7	1.6	1.6	1.6
6600	1.5	1.5	1.5	1.5	1.4	1.4	1.4	1.3	1.3	1.3	1.2	1.2	1.2	1.2	1.1	1.1	1.1	1.0	1.0	1.0
6720	0.9	0.9	0.9	0.9	0.4	−0.3	−0.9	−0.8	−0.5	−0.1	−0.1	−0.7	−1.0	−1.1	−1.0	−0.9	−0.8	−0.7	−0.6	−0.3
6840	0.2	−0.3	−1.0	−1.3	−1.0	−0.6	0.1	0.9	1.6	2.2	2.1	1.9	1.7	1.5	1.4	1.2	1.0	0.8	0.6	0.4
6960	0.3	0.1	−0.1	−0.3	−0.5	−0.6	−0.8	−1.0	−1.2	−1.4	−1.5	−1.7	−1.9	−2.1	−2.3	−2.5	−2.6	−2.8	−2.0	−0.5
7080	0.1	0.4	0.4	0.4	0.4	0.3	−0.5	−1.4	−1.3	−1.0	−0.3	0.3	1.0	1.6	0.8	−1.5	−1.5	−1.3	−1.2	−0.6
7200	0.0	0.0	0.1	0.2	0.2	0.2	0.3	0.4	0.4	0.5	0.5	0.6	0.6	0.7	0.7	0.8	0.9	0.9	1.0	1.0
7320	1.1	1.1	1.2	1.2	1.3	1.3	1.4	1.4	1.5	1.5	1.6	1.7	1.9	2.3	2.7	2.0	1.3	0.6	−0.1	−0.3
7440	−0.1	0.4	0.6	0.7	0.6	0.5	0.3	0.2	0.5	0.6	0.5	0.4	0.2	0.1	0.0	−0.2	−0.3	−0.3	−0.2	−0.2
7560	−0.2	−0.1	−0.1	0.0	0.0	0.0	0.1	0.1	0.2	0.2	0.2	0.3	0.3	0.4	0.4	0.4	0.5	0.5	0.6	0.6
7680	0.6	0.7	0.7	0.8	0.8	0.8	0.9	0.6	0.1	−0.5	0.5	0.0	−1.3	−1.2	−0.7	0.2	1.1	0.7	0.0	−1.0
7800	−2.0	−2.3	−2.2	−2.0	−1.5	−0.4	0.5	1.3	1.5	1.3	1.0	0.8	0.6	0.4	0.2	0.0	−0.2	−0.4	−0.6	−0.5
7920	0.0	−0.1	−0.4	0.0	0.1	−0.8	0.4	0.7	0.6	0.5	0.4	0.3	0.2	0.2	0.1	0.0	−0.1	−0.2	−0.3	−0.4
8040	−0.2	1.3	1.2	−0.1	−0.1	0.3	0.0	−0.9	−0.5	−1.7	−0.8	−0.3	0.0	0.3	0.6	0.6	0.5	0.3	0.1	−0.1
8160	−0.3	−0.4	−0.6	−0.8	−1.0	−1.2	−1.4	−1.5	−1.7	−1.9	−2.1	−2.2	−1.6	−1.4	−1.1	0.3	0.5	−0.2	0.0	−0.3
8280	−0.1	0.8	0.7	−0.6	0.9	1.1	0.9	0.7	0.5	0.4	0.3	0.2	0.1	−0.1	−0.2	−0.3	−0.4	−0.1	0.3	0.2
8400	0.0	−0.2	0.2	0.2	−0.7	−0.5	0.3	0.5	0.0	0.5	0.6	−1.0	−1.2	0.3	1.2	1.2	0.5	−0.3	−1.1	−1.9
8520	−2.6	−2.0	0.2	1.2	0.8	0.5	0.1	−0.2	−0.6	−0.9	−1.0	−0.3	0.7	0.8	0.1	0.5	−0.2	−1.2	−0.5	0.9
8640	0.6	0.6	1.0	1.4	1.4	0.3	0.3	0.5	0.4	0.2	0.1	−0.1	−0.3	−0.5	−0.7	−0.9	−0.7	−0.3	0.0	0.3
8760	0.4	0.2	0.8	0.1	−0.5	0.3	1.3	0.6	0.5	0.1	−1.7	−1.2	0.6	0.9	0.6	0.4	0.2	0.1	0.0	−1.4

Note: Entries are listed in degrees, a positive value means the parachute is further east than Huygens.

altitude. In images taken at 22 and 20 km altitude, this haze layer appears too weak to be clearly identifiable.

With the function fixed, we allowed the orientation of each image to vary until we got the best fit by the least-squares method. This gave us a set of orientation angles for each SLI image. The accuracy of the pitch and roll is probably about 2° on average. The accuracy for the azimuth is not as good. This seems unavoidable for the images at lower altitude. For images taken at higher altitude, above 75 km, or before MT 1500, we applied a separate method to obtain azimuths of higher accuracy.

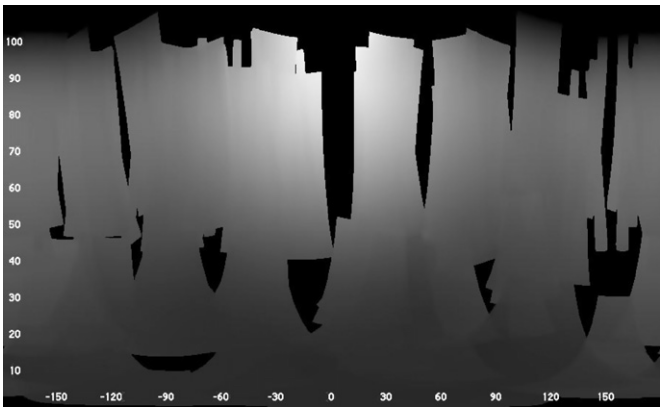

Fig. 4. The sky mosaic for all images taken on the main parachute (above 110 km altitude). The azimuth goes from 180° to the left of the Sun to 180° to the right of the Sun. The nadir angle goes from 0° to 110° (20° above the horizontal direction). Areas not imaged are left black. In the vertical direction, the brightest area is just below the horizontal direction. The brightest spot is below the Sun.

For images taken above about 75 km altitude, the area near the horizon is the brightest area in the SLI frames. Looking further down, the sky is fainter because less solar radiation reaches the lower altitude. Looking up, the sky is also fainter since the haze does not reach the optically thick limit in this direction. Thus, for each azimuth, there is a maximum sky brightness, which can be accurately measured. At a specific altitude, there is a unique function of the maximum sky brightness as a function of azimuth (cf. Fig. 5). This function varies with altitude, but only weakly. With decreasing altitude, the decreasing solar radiation seems to be almost perfectly compensated by the increasing brightness due to the increasing optical depth along the line of sight. Using all SLI and SLI strip data above 75 km altitude, we could determine this function so accurately, that we could retrieve the azimuths of images as accurately as 3°, where the sky brightness changes strongly with azimuth, which is within 90° of the solar azimuth.

5. Measuring Huygens' rotation

5.1. AGC gain features

In this section, we focus on data which constrain the azimuth as a function of time. Our goal is to know the azimuth for each moment during the descent. The most suitable data set for this purpose is the strength of the Huygens probe relay signal, which was measured by the Automatic Gain Control (AGC) of the Huygens receiver aboard Cassini. The gain was recorded eight times per second on a logarithmic scale with high precision (cf. Appendix A, housekeeping data).

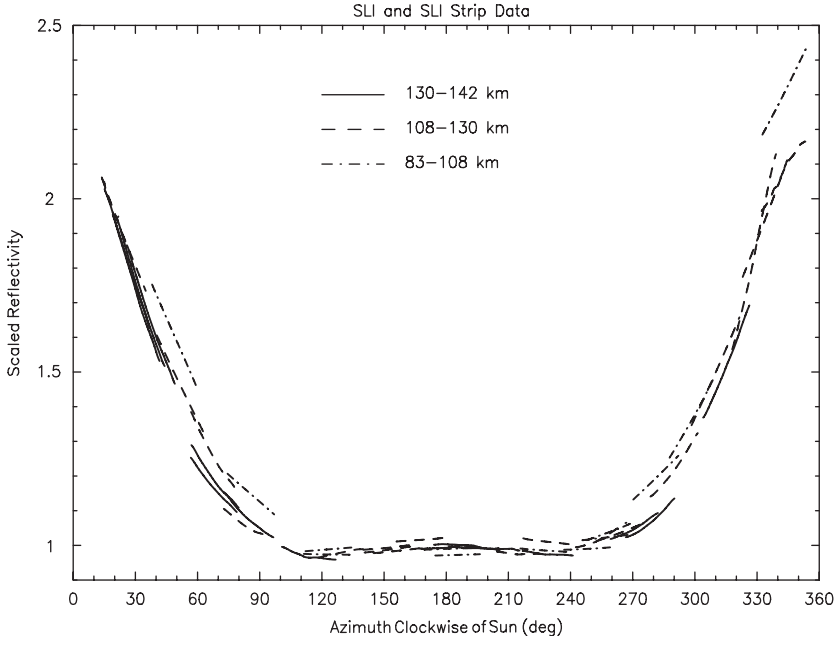

Fig. 5. The maximum reflectivity (over all nadir angles) as function of azimuth relative to the solar azimuth for SLI images and SLI strip images at high altitude, scaled to unity at the anti-Sun azimuth. The solid, dashed, and dashed-dotted curves indicate that the shape of the reflectivity function varies only slowly with altitude. Therefore, the steep sections within 90° of the Sun can be used to constrain azimuths of these images.

Due to the specific shape of the two Huygens transmitting antennae gain patterns, the AGC signal strength measurements vary as a function of rotation angle and probe aspect angle (i.e. the angle between the rotational axis and the direction to Cassini), as shown in Fig. 9 of Kazeminejad et al. (2004).

Because of the antenna pattern of Huygens, the gain has a complicated structure as a function of rotation angle and aspect angle, the angle between the rotational axis and the direction to Cassini. Since the aspect angle typically changed little on short time scales, the gain was strongly correlated with the rotation angle.

For most of the descent, from around MT 1500 (76 km altitude) to landing, the AGC signal is clearly periodic, and the number of rotations of Huygens can be easily counted. There is some periodic structure before MT 1500 as well, but its interpretation is not trivial. Since we got accurate azimuth data for this interval in the previous section, we did not spend much effort on the AGC data before MT 1500. During this time, Cassini was almost overhead as seen from Huygens, where rotational features of the gain are less distinct. Furthermore, tip and tilt of Huygens change measured azimuths very much when Cassini is close to overhead.

We divided all AGC data into quarter rotations. We also averaged the AGC data of the same rotation angle over 10 consecutive rotations. We then compared the shape of a single data set of a quarter rotation with the average of the same quarter over the previous 10 rotations and with the average over the following 10 rotations. We shifted the single data set until we obtained a least-squares fit. After iterating this procedure many times, we had four MTs for each rotation, one for every 90° of rotation. We then slightly smoothed this data set so that rotational accelerations would be smaller, because some of the apparent accelerations over short time scale are not due to actual changes of the rotation of Huygens, but due to a swinging probe.

This method gave reliable rotational data over the course of several rotations. However, over the course of some 50 rotations, the AGC gain features changed so much that the data could not be well compared, which means that rotational data derived from AGC gain could be biased by a small drift. Furthermore, this method gave only relative azimuths. Therefore, we needed to add further data, discussed in Sections 5.2 and 5.3.

Fig. 6 displays the shape of the AGC gain over the course of the descent, as Cassini moves from almost overhead towards the horizon. While the motion of Cassini is smooth, the shape of the AGC gain does not seem to change smoothly. However, once we included the tilt of Huygens as discussed in Section 10.3, then the rapid changes of the AGC gain features corresponded well with rapid changes of the aspect angle. Most noticeable is the sudden appearance of a regular pattern near rotation number 100 (Fig. 6) with exactly corresponds with the rapid change of aspect angle due to the minimum wind speed at that layer.

The only free parameter in this method is the amount of smoothing. If the amount of smoothing were chosen too small, most of the high-frequency features in the inferred rotational profile would be noise. If the amount of

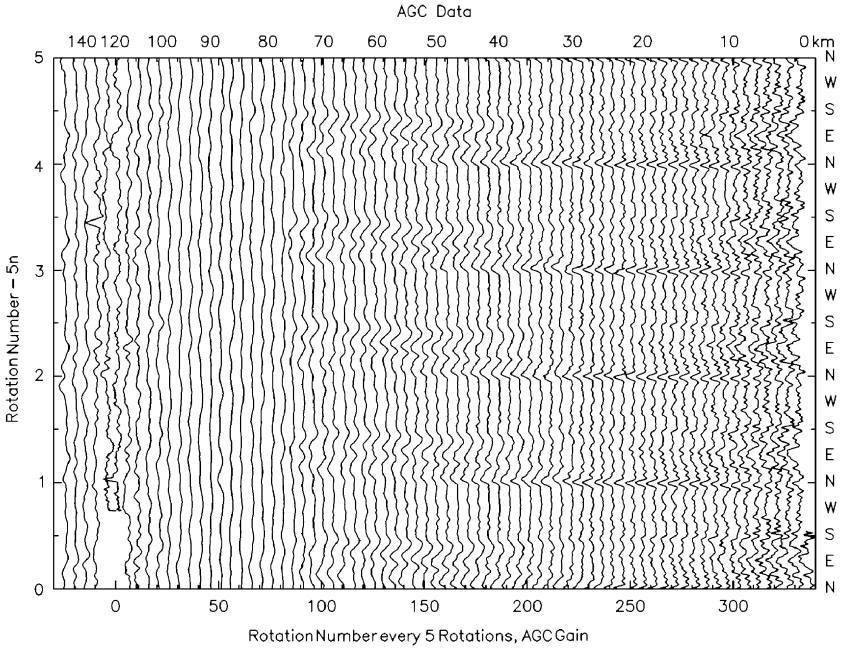

Fig. 6. The AGC gain, plotted towards the right as function of the Huygens rotation. Each section of five rotations is shifted to the right with respect to the previous section. Before rotation zero, Huygens was rotating counterclockwise, and time goes from top to bottom. After the turn-around point at rotation 0.7, Huygens was rotating clockwise and time goes from bottom to top. Starting near rotation 100, features are consistent enough to allow tracking of the rotation of Huygens through feature matching. Altitudes are given on top. The cardinal directions are given at the right side.

smoothing were chosen too large, many of the real, medium-frequency features would be smoothed out. We chose the amount of smoothing in order to get the best correlation with other methods described in Sections 5.2 and 5.3. This method gives the largest rotational irregularities on the scale of several rotations accurate to about 1%. Rotational irregularities on the scale of less than one rotation were still retrieved by this method, but at a reduced level. Among the more than 100 rotational irregularities detected, about 95% are estimated to be real, those with amplitudes of 2–180°.

A similar study of the rotation of Huygens was done by Lebreton et al. (2005). We will compare results in Section 10.2. Our azimuth function is listed in Table 3. It is not only based on AGC data, but also on other data discussed in Sections 5.2 and 5.3. After MT 2100 (57 km altitude), linear interpolation over 10-s intervals listed in Table 3 retrieves the nominal curve to better than 1°. Before MT 2100, there are a few intervals where quadratic or cubic interpolation would be needed for the same precision. However, during those events, the accuracy is maybe 4° instead of the typical 2°, so that linear interpolation is still better than the accuracy.

5.2. The ULVS rotation function

The Upward-Looking Visible Spectrometer (ULVS) had a field of view of almost the whole sky within 90° of the DISR azimuth, except for a central vertical shadow bar (cf. Table I in Tomasko et al., 2002). The relative sensitivity over the field of view was measured in the laboratory. If the sky brightness as function of azimuth and zenith angle is known from a model, the ULVS data as function of azimuth can be predicted, which we will call the ULVS rotation function. Since one of the earliest, reliable haze models was done at 830 nm wavelength, we compared the ULVS data at this wavelength with predictions from our best haze model. For each altitude, we used the maximum and minimum predicted data numbers to linearly scale the rotation function to a minimum of zero and maximum of unity. In these scaled data numbers, the rotation function stays almost constant with altitude, and observations of many altitudes can be easily compared (Fig. 7).

Using estimates of the azimuths of the data based on Section 5.1, the data and predictions agree roughly except for offsets in azimuth, which then can be used to shift the azimuths to an accurate absolute scale. We divided the 246 ULVS data points during the descent into about eight altitude ranges with some 30 data points each. Because only a fraction of the data points fall into the section where the rotation function is steep and where azimuths can be best constrained, and because individual data points may be off from the curve by several degrees due to non-zero pitch and roll, some 30 data points are required to achieve a good constraint on the azimuth.

The data points before MT 1500 (76 km altitude) were very consistent with the azimuth determination in Section 4, aside from a symmetric scatter due to pitch and roll. The data points after MT 1500 constrained the arbitrary offsets of azimuths from AGC data described in Section 5.1. While the AGC provided the rotational structure at short time scales, the ULVS provided the rotational structure at long time scales to 1° accuracy, so that the surface mosaic could be oriented with respect to north to about 1° accuracy. On intermediate time scales, the AGC and ULVS data were consistent with each other. Of course, we considered the variation of azimuths of the Sun and Cassini for this comparison.

We also checked how sensitive our result is to the assumed sky brightness model. For example, we fitted the data with a model from a very different altitude. In those cases, the best fit changed by less than 1°, indicating that accurate knowledge of the sky brightness was not critical in this context. This was expected, since in each altitude section, there were similar numbers of data points near the ascending and descending part of the rotation function.

In this context, we should mention that the timing of DISR data comes from the Huygens clock, while the timing of AGC data comes from the Cassini clock. If both clocks are off by a second or two, this would offset azimuths of Section 5.1 by amounts proportionally to the instantaneous rotational rate. We checked for such a correlation, and we found the best fit for an apparent clock offset of 2.0 ± 0.2 s, which we adopted. We also looked just at the single most prominent feature in the AGC data, the minimum gain. Without a clock offset, this feature would need to shift in azimuth by 90° between the regions of fast and slow rotation, which seems unrealistic (Fig. 8). For an apparent clock offset of 2.0 ± 0.2 s, this feature remains roughly stationary, especially after rotation 100 (Fig. 8), where the AGC gain features are sharp enough to allow reliable measurements.

Other observations also indicate a clock offset of similar size. For example, the HASI accelerometers found that Huygens impacted at MT 8869.8 and came to rest shortly thereafter (Fulchignoni et al., 2005), while the AGC data changed from variable to almost constant at MT 8872.8. Note that our 2.0 s offset corresponds to the apparent offset, while the real offset was only about 1.8 s, because the light travel time between Huygens and Cassini was 0.2 s.

5.3. The ULIS rotation function

The Upward-Looking Infrared Spectrometer (ULIS) and ULVS had similar fields of view, except that the ULIS had no vertical central shadow bar. Thus, azimuths can be constrained by ULIS data in a similar way as for the ULVS data shown in the previous section. During most of the descent, ULIS exposures consisted of many shutter-open, shutter-close cycles, which gave only very weak constraints on the azimuths. Only during the last 11 min before landing (<3 km altitude) was the chip read out after each shutter cycle. We analyzed the 18 measurements made during this

Table 3
Azimuth function of Huygens

MT (MT+)	0	10	20	30	40	50	60	70	80	90	100	110
0	31.530	30.363	29.196	28.030	26.874	25.753	24.668	23.622	22.613	21.638	20.694	19.776
120	18.884	18.017	17.173	16.352	15.552	14.771	14.008	13.265	12.542	11.840	11.161	10.503
240	9.864	9.244	8.640	8.052	7.481	6.930	6.404	5.904	5.431	4.987	4.570	4.181
360	3.818	3.479	3.162	2.865	2.585	2.322	2.078	1.852	1.647	1.464	1.303	1.164
480	1.046	0.948	0.870	0.809	0.766	0.740	0.730	0.735	0.756	0.794	0.848	0.918
600	1.005	1.108	1.227	1.360	1.509	1.672	1.850	2.043	2.251	2.472	2.706	2.954
720	3.214	3.488	3.775	4.076	4.390	4.718	5.060	5.415	5.784	6.166	6.562	6.973
840	7.397	7.834	8.284	8.747	9.222	9.710	10.211	10.723	11.255	11.823	12.435	13.063
960	13.714	14.420	15.181	15.996	16.872	17.787	18.733	19.704	20.697	21.714	22.757	23.830
1080	24.935	26.076	27.256	28.476	29.733	31.026	32.354	33.718	35.117	36.550	38.016	39.520
1200	41.060	42.635	44.237	45.857	47.483	49.102	50.709	52.304	53.892	55.472	57.045	58.615
1320	60.182	61.746	63.298	64.830	66.329	67.787	69.204	70.584	71.937	73.274	74.602	75.925
1440	77.240	78.541	79.822	81.078	82.309	83.516	84.701	85.867	87.016	88.150	89.278	90.392
1560	91.468	92.499	93.502	94.481	95.450	96.436	97.424	98.401	99.366	100.331	101.270	102.173
1680	103.076	103.999	104.902	105.818	106.712	107.563	108.416	109.262	110.076	110.871	111.669	112.485
1800	113.284	114.076	114.859	115.652	116.437	117.203	117.965	118.740	119.536	120.337	121.101	121.853
1920	122.605	123.352	124.087	124.811	125.538	126.236	126.957	127.665	128.394	129.121	129.810	130.502
2040	131.214	131.909	132.620	133.321	133.985	134.658	135.335	135.983	136.631	137.284	137.931	138.566
2160	139.167	139.763	140.361	140.961	141.548	142.114	142.648	143.161	143.689	144.210	144.727	145.248
2280	145.777	146.296	146.800	147.285	147.757	148.241	148.728	149.200	149.656	150.101	150.533	150.958
2400	151.396	151.838	152.283	152.729	153.174	153.612	154.033	154.440	154.856	155.280	155.702	156.123
2520	156.545	156.973	157.412	157.860	158.314	158.783	159.240	159.682	160.120	160.556	160.985	161.428
2640	161.865	162.292	162.713	163.125	163.530	163.936	164.366	164.829	165.290	165.735	166.171	166.608
2760	167.057	167.516	167.975	168.457	168.942	169.420	169.876	170.338	170.802	171.248	171.681	172.113
2880	172.546	172.978	173.411	173.856	174.319	174.786	175.229	175.653	176.068	176.473	176.882	177.319
3000	177.777	178.243	178.690	179.132	179.571	180.009	180.452	180.902	181.321	181.743	182.156	182.565
3120	182.970	183.377	183.787	184.161	184.519	184.909	185.288	185.665	186.045	186.435	186.822	187.211
3240	187.597	187.971	188.316	188.662	189.026	189.443	189.865	190.250	190.621	190.991	191.366	191.752
3360	192.161	192.590	193.019	193.451	193.878	194.279	194.658	195.027	195.396	195.758	196.125	196.505
3480	196.908	197.323	197.743	198.157	198.548	198.909	199.251	199.606	199.979	200.336	200.693	201.068
3600	201.475	201.895	202.293	202.701	203.115	203.517	203.905	204.306	204.692	205.079	205.466	205.870
3720	206.255	206.638	207.030	207.411	207.821	208.217	208.588	208.954	209.301	209.621	209.931	210.293
3840	210.654	211.008	211.365	211.697	211.996	212.250	212.523	212.853	213.263	213.685	214.073	214.445
3960	214.863	215.291	215.714	216.159	216.641	217.128	217.596	218.038	218.459	218.861	219.245	219.623
4080	220.003	220.392	220.768	221.138	221.498	221.845	222.170	222.470	222.732	223.006	223.323	223.658
4200	224.007	224.358	224.722	225.080	225.421	225.762	226.089	226.404	226.731	227.064	227.393	227.665
4320	227.920	228.193	228.483	228.790	229.095	229.389	229.661	229.942	230.243	230.534	230.829	231.123
4440	231.417	231.720	232.023	232.335	232.653	232.972	233.290	233.612	233.938	234.269	234.607	234.950
4560	235.299	235.642	235.973	236.282	236.586	236.890	237.193	237.496	237.802	238.122	238.458	238.809
4680	239.150	239.479	239.792	240.113	240.441	240.768	241.093	241.418	241.744	242.078	242.420	242.737
4800	243.050	243.363	243.654	243.939	244.243	244.546	244.843	245.147	245.444	245.722	246.003	246.284
4920	246.564	246.841	247.097	247.316	247.496	247.668	247.842	248.002	248.180	248.385	248.627	248.895
5040	249.138	249.379	249.636	249.898	250.143	250.383	250.631	250.888	251.155	251.433	251.718	252.016
5160	252.332	252.650	252.965	253.261	253.550	253.841	254.118	254.383	254.634	254.884	255.126	255.369
5280	255.623	255.899	256.185	256.482	256.771	257.062	257.359	257.651	257.936	258.205	258.471	258.742
5400	259.015	259.289	259.563	259.836	260.113	260.392	260.664	260.933	261.205	261.480	261.760	262.032
5520	262.291	262.551	262.811	263.073	263.336	263.614	263.906	264.192	264.475	264.753	265.018	265.267

5640	265.523	265.790	266.069	266.359	266.638	266.910	267.188	267.462	267.722	267.978	268.241	268.501
5760	268.759	269.014	269.270	269.540	269.815	270.085	270.362	270.638	270.908	271.175	271.437	271.691
5880	271.947	272.206	272.466	272.732	272.997	273.260	273.527	273.802	274.077	274.351	274.627	274.904
6000	275.184	275.456	275.711	275.957	276.199	276.440	276.684	276.927	277.174	277.442	277.707	277.963
6120	278.233	278.515	278.791	279.059	279.327	279.597	279.865	280.126	280.375	280.619	280.869	281.113
6240	281.355	281.596	281.840	282.094	282.357	282.613	282.867	283.122	283.378	283.634	283.889	284.132
6360	284.369	284.607	284.845	285.089	285.337	285.591	285.851	286.109	286.361	286.604	286.835	287.060
6480	287.269	287.470	287.675	287.899	288.130	288.354	288.584	288.826	289.068	289.314	289.556	289.795
6600	290.032	290.265	290.501	290.745	290.983	291.212	291.435	291.651	291.864	292.082	292.305	292.525
6720	292.754	292.980	293.202	293.425	293.661	293.895	294.116	294.336	294.550	294.751	294.955	295.171
6840	295.389	295.608	295.837	296.068	296.279	296.494	296.720	296.952	297.190	297.434	297.682	297.934
6960	298.195	298.450	298.691	298.924	299.152	299.377	299.603	299.828	300.044	300.251	300.462	300.664
7080	300.867	301.068	301.265	301.477	301.697	301.921	302.143	302.363	302.584	302.792	302.997	303.209
7200	303.421	303.617	303.817	304.019	304.219	304.418	304.613	304.806	305.002	305.199	305.399	305.602
7320	305.810	306.020	306.233	306.446	306.659	306.870	307.076	307.280	307.484	307.680	307.878	308.076
7440	308.279	308.505	308.717	308.908	309.099	309.293	309.472	309.652	309.837	310.026	310.219	310.442
7560	310.640	310.867	311.083	311.293	311.508	311.730	311.952	312.170	312.388	312.612	312.837	313.056
7680	313.270	313.478	313.680	313.880	314.081	314.277	314.470	314.657	314.842	315.023	315.214	315.403
7800	315.576	315.759	315.952	316.149	316.356	316.551	316.739	316.923	317.097	317.265	317.437	317.615
7920	317.797	317.990	318.199	318.413	318.622	318.828	319.030	319.225	319.421	319.623	319.827	320.021
8040	320.205	320.387	320.571	320.755	320.941	321.129	321.319	321.514	321.715	321.915	322.109	322.301
8160	322.492	322.680	322.869	323.067	323.273	323.476	323.677	323.866	324.063	324.223	324.381	324.551
8280	324.726	324.912	325.087	325.265	325.446	325.631	325.822	326.019	326.226	326.417	326.581	326.735
8400	326.886	327.059	327.245	327.439	327.632	327.823	328.012	328.201	328.385	328.570	328.766	328.964
8520	329.167	329.372	329.564	329.746	329.929	330.111	330.282	330.461	330.656	330.861	331.069	331.269
8640	331.452	331.621	331.791	331.971	332.151	332.326	332.500	332.680	332.863	333.046	333.217	333.394
8760	333.581	333.774	333.981	334.167	334.349	334.525	334.695	334.862	335.035	335.212	335.384	335.536

Note: Entries are listed in full rotations for DISR (Huygens z-axis) east of north ($0.000 = \text{north}, 0.250 = \text{east}, 0.500 = \text{south}, 0.750 = \text{west}$).

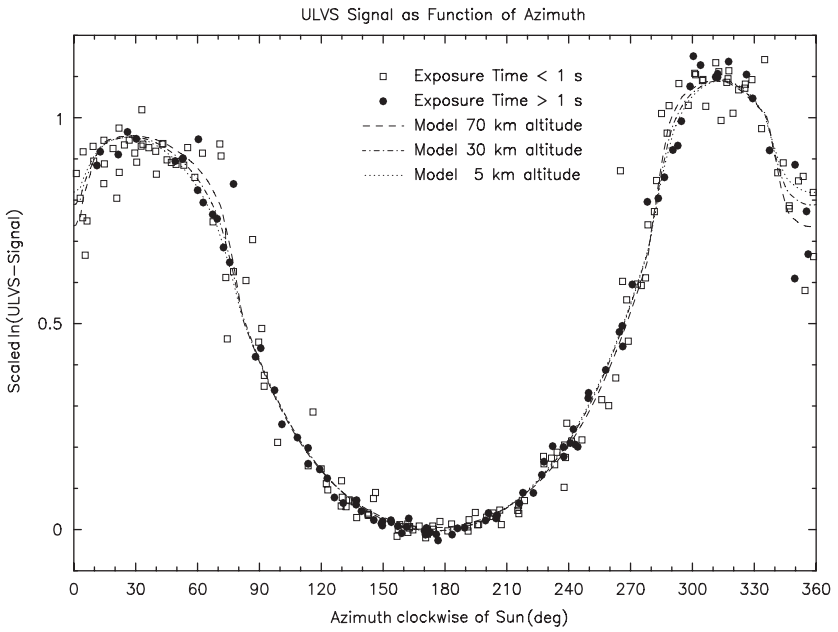

Fig. 7. Scaled ULVS signal at 830 nm wavelength as function of azimuth relative to the solar azimuth. The signal was linearly scaled by a smooth function of altitude for this figure. The three curves represent expected functions for three altitudes based on our best haze model. Exposures with long exposure times seem to better fit the expected curves, because the swing period of Huygens was fast enough to smear out deviations due to tilt for exposure times larger than about a second. Shown are all 246 ULVS measurements before landing.

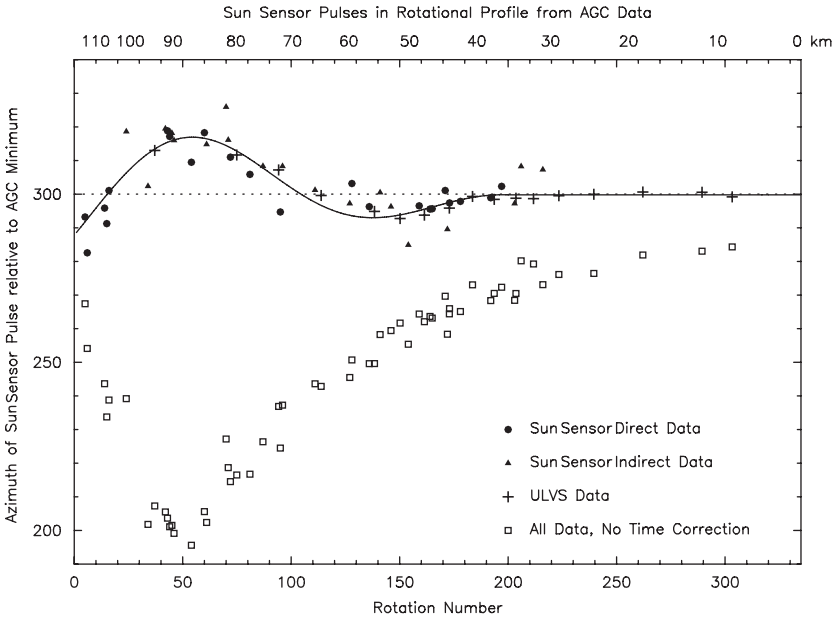

Fig. 8. Azimuth of the Sun Sensor pulses if azimuth zero were defined as the AGC feature corresponding to the minimum gain. Filled circles are transmitted timings. Triangles are inferred timings from error messages. Also shown are ULVS data using the ULVS rotation function (crosses). The curve is the adopted offset. Open squares show all data before the 2-s timing offset between Huygens and Cassini was taken into account. Altitudes are listed at the top every 20 km, but the tick marks correspond to rotation numbers.

time interval and compared them with predictions calculated from models of the sky brightness at 938 nm wavelength. For the predictions, we took into account the exposure times (1 and 8 s) which correspond to rotation angles of Huygens of as much as 50° (Fig. 9).

The best fit yielded absolute azimuths 2° off from the determination using the ULVS. Our adopted azimuths for the last stages of the descent are half way inbetween both values.

6. The radar image

In order to attach longitudes and latitudes to our surface mosaic, we used the Cassini radar image from the T8 fly-by

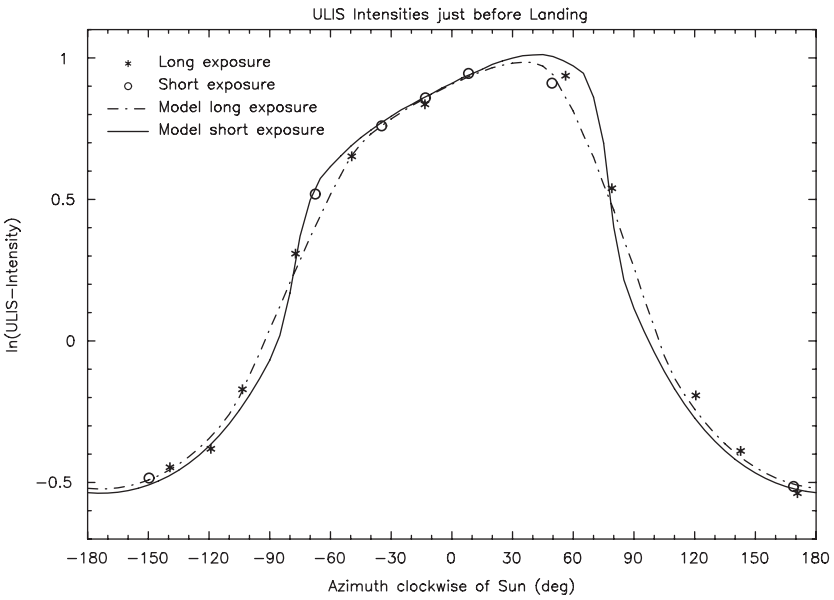

Fig. 9. Measured intensities of the ULIS during the last 11 min of the descent (<3 km altitude). Open circles are short exposures and are expected to follow the solid curve, based on our best haze model. Stars indicate long exposures and are expected to follow the smoothed dashed-dotted curve.

(Lunine et al., 2007). This radar image has coordinates attached to it accurate to about 0.02° or 1 km, while our comparison of features was estimated to be accurate to about 5 km. We determined Huygens landing coordinates of 167.6° east and 10.2° south, to 0.1° accuracy, in agreement with Lunine et al. (2007). The correlation was mostly based on two dark sand dunes north of the landing site. The dunes and some other possible large-scale features between the landing site and the dunes gave a good correlation for coordinates of $167.59 \pm 0.10°$ and $10.19 \pm 0.05°$. A small, almost circular feature half way between the landing site and the dunes gave a much tighter constraint: $167.69 \pm 0.02°$ and $10.25 \pm 0.02°$, which also worked for a few other small features. However, among the hundreds of possible features, a few of them fit for almost every assumed landing coordinates. Thus, a determination to better than 0.1° probably needs to wait for another radar observations, expected later in the Cassini mission.

7. Sun Sensor data

7.1. Data for the central slit

The DISR Sun Sensor had three slits tilted with respect to each other to record the passing of the Sun (Fig. 10). The central slit was aligned with the x–z plane of Huygens (cf. Fig. 14 in Tomasko et al., 2002). A central slit timing corresponded to DISR pointing at the azimuth of the Sun, at least for zero roll. We received timings of 69 rotations, a small fraction of the possible 360 timings during the descent. For the last 120 rotations, below 30 km altitude, the Sun Sensor was not sensitive enough due to a combination of three effects: the haze was thicker than expected, the Sun Sensor assembly got colder than expected, and the Sun Sensor silicon had a stronger temperature dependence than expected. The design margin of the Sun Sensor was large enough to handle two of these effects, but not all three. For the rest of the descent, the Sun Sensor lost lock 28 times, which will be discussed in Section 7.3.

We compared the 69 measurements with the expected times based on the azimuth information from Section 5. The azimuths from the Sun Sensor data were off by 5° rms from the azimuths as determined earlier. This difference corresponds to a 3° rms roll angle. Such a roll is consistent with our analysis of Section 4. The average azimuth for the 69 data points is off by 1° from the expected average based on results from Section 5. Since a sample of 69 observations with a scatter of 5° can statistically only give the average to about 1° accuracy, this result is a confirmation of the accuracy of our absolute azimuth determination to about 1° (Fig. 8).

7.2. Explanation of error events

We expected the Sun to cross the three symmetrical slits in a regular way, with a similar spacing between both time intervals. To our surprise, this was not the case at all. During the time interval between the three slit crossings, typically about 1 s, the rotation or swing of Huygens must have changed completely, sometimes so strongly that it knocked the Sun Sensor out of lock. While the rotation around the vertical axis was variable on the time scale of a minute, it is very hard to image it could change significantly within a fraction of a second. Thus the only remaining possibility is a swing of Huygens.

The Sun Sensor was extensively tested on a rotating and swinging platform with various combinations of rotational and swinging rates, but it never lost lock as it did 28 times during the descent. However, we never applied swinging

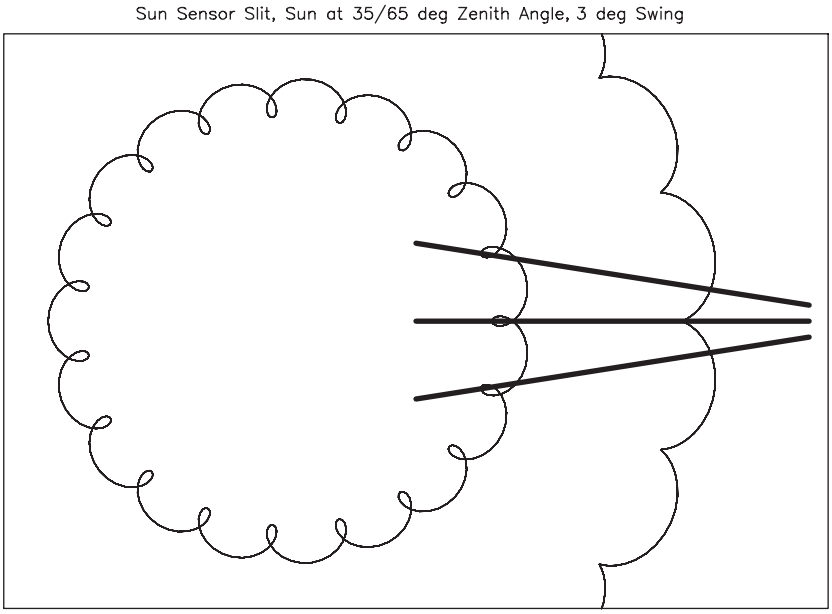

Fig. 10. The path of the Sun with respect to the three slits of the Sun Sensor for 35° (interior curve) and 65° (exterior curve) solar zenith distance, the design limits. The actual solar zenith distance was 36° on average. A swing of 3° amplitude is assumed with 20 periods during one Huygens rotation. Note that near 35° zenith angle, multiple slit crossings can occur, which decrease the performance of the Sun Sensor.

rates above 6°/s, the design limit for Huygens. Simulations of the software of the Sun Sensor indicate that it could loose lock at swinging rates well above 6°/s. Other observations, such as smeared images (Section 2.1), indicate higher than expected swinging rates.

We divided the Sun Sensor data into two sections, the section on the main parachute, where it lost lock three times, and the section on the stabilizer, where it lost lock 25 times. On the main parachute, the rotation of Huygens stopped and continued in the opposite direction. While the Sun Sensor worked equally well for both directions, it was not designed for a non-rotating probe, and thus went out of lock near that time. Furthermore, the strong structure in the profile of the zonal Huygens speed (Bird et al., 2005) at those altitudes caused the probe to tilt back and forth. This tilting can almost explain the remaining two error events of the Sun Sensor on the main parachute. Either there was a little more small-scale structure in the horizontal Huygens speed profile, not resolved by the DWE, or Huygens had a high-frequency swing due to other reasons with an amplitude of less than 1°, much less than the low-frequency tilting of up to 15°. With only two events, one cannot say too much, except that the tilting of Huygens was close to what would be expected from the Huygens speed profile.

For the stabilizer, the story is very different. Expected tilting based on the Huygens speed profile was far too low to cause any one error event of the Sun Sensor, yet 25 error events were recorded. Something else must have caused Huygens to swing. In order to understand the swinging of Huygens during this phase, between 110 and 30 km altitude, we first consider the theoretically expected swing modes of the Huygens–parachute system.

7.3. Theoretical swing modes

The Huygens–parachute system has two swing modes. In the slow swing mode, the whole system swings like a rigid pendulum of 12 m length with a period near 20 s. For typical tilt angles of 5° derived in Section 4, the swinging rate peaks near 0.1°/s, far below the design limit of 6°/s, far too low to affect the Sun Sensor. Furthermore, damping of this swing occurs on a much faster time scale than one swinging period.

In the other swing mode, sometime called scissors or "half-scissors" mode, Huygens and the parachute are almost stationary, while the swinging amplitude is greatest where the three bridal lines from Huygens meet. We used data from the Huygens User Manual Description (cf. Appendix A, housekeeping data), particularly a mass of 200 kg, a probe inertia of 24 kg m^2, increased to 30 kg m^2 due to the swivel mass of 0.4 kg, and a distance to the confluence of the three bridal lines of 4 m, and we used Titan's gravity of 1.3 m/s^2 and an estimated weight of 80% carried by the parachute. This gave a swing period of 1.2 s, assuming that the descent speed was fast enough so that the parachute aligned itself above the swivel within a fraction of the swing period, which was the case early during the stabilizer descent. Basically, only the bottom part of the scissors rotated. Near Titan's surface, the descent speed was so slow that the parachute remained roughly above Huygens, not above the swivel. Basically, both ends of the scissors remained stationary. This gave an extra pull on the swivel, reducing the period to 1.0 s. For the interpretation of Sun Sensor data, which were taken above 30 km altitude, a swing period near 1.2 s should be applicable.

Our estimation is in good agreement with Underwood et al. (private communication) who calculated a swing frequency of 0.80 Hz for Huygens on the stabilizer parachute. They also noted that the frequency should be slightly higher than 0.80 Hz because of the relatively short parachute. They interpret the system accelerometer data as showing strong evidence of this high-frequency swing mode during the stabilizer phase, but they also note that during the main-parachute phase, this swing mode with similar frequency must have been much less excited, in good agreement with our findings.

Any swing in this swing mode should have been damped by the parachute within one or a few periods. This means that keeping the system swinging required constant excitation. This also means that the swinging is not expected to have been a perfect harmonic oscillation, but possibly a more irregular state, such as a swing of variable amplitudes and somewhat variable periods near 1.2 s. In the following model, we will assume a harmonic swing, but we consider in the interpretation that this is an idealized model. During each rotation we assume a swing where the axis of Huygens rotated at constant amplitude around the vertical with a period of 1.2 s, like a precessing whipping top. From one rotation to the next, the amplitude and the phase of the swing during the central slit crossing was allowed to change.

First, we show the apparent path of the Sun on the Sun Sensor slit system for a swing amplitude of 3° (16°/s swing rate) and a rotational rate of Huygens of 2.5 RPM (Fig. 10). This rotational rate was typical for altitudes between 50 and 30 km. Fig. 10 shows the paths for the design limits of the solar zenith angle, which were 35° and 65°. In the 65° case, the Sun moves orderly across the slits. In the 35° case, the Sun makes loops that can cause triple crossings of the same slit, which the Sun Sensor was not designed for. The average solar zenith angle during the descent was 36°, close to the edge of the design interval. Note that for swing rates within the design limit of 6°/s, the solar path would not have any loops.

7.4. Data from all three slit timings

Now, we look at individual Sun Sensor data. For each rotation, we use the rotational rate determined in Section 5. This provides the expected slit crossing time between the first and third pulse, which is based on zero tilt of Huygens. We now set the swing amplitudes at 3°, 6°, and 9° (16°, 32°, and 48°/s swing rate), and let the phase of the swing vary. This gives a range of possible slit crossing times between the first and third pulse. In Fig. 11, we compare these ranges with actual data of all our 45 observations with triple-slit timings (solid dots) and the remaining partial data (open symbols). Wherever curves are tightly spaced near the data points, one cannot say too much because expected slit crossing times are uncertain by a few percent and because the swing is not expected to be perfectly harmonic. However, many data points are located where curves have significant spacing to determine approximate swing rates. Typical swing rates were 10–20°/s, while a few observations require occasional swing rates of about 40°/s.

For example, let us consider the data point at the lower right with an expected slit crossing time of 2.0 s and an observed one of 0.40 s. The rotational rate was 2.8 RPM, which should have moved the Sun at a rate of 10°/s in 2 s

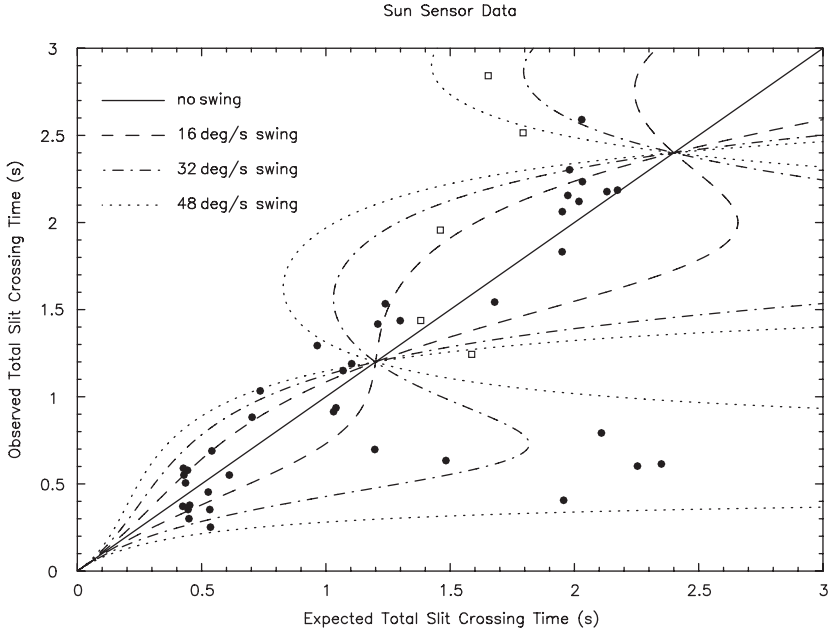

Fig. 11. Observed slit crossing times for the Sun Sensor versus expected times, based on the rotational rate of Huygens. The solid line shows the identity for no swing of Huygens. The dashed, dashed-dotted, and dotted lines show the possible range for swing amplitudes of 3°, 6°, and 9°, respectively. All calculations assume a swing period of 1.2 s. Solid dots indicate primary timing data. Open squares indicate timings inferred from time stamps of error messages.

across the 20° distance between slit 1 and slit 3. Actually, the timing data indicate a speed of five times as fast, of which 40°/s must be due to swing. Due to tilt of Huygens and the tilt between the slits, the actual distance could have been between 18° and 22°, which constrains the swing rate to 35–45°/s. This is really a minimum swing rate for that instant since the Sun Sensor measured only the component of the swing rate perpendicular to the central slit. Considering that a few of the 45 primary data points indicate swing rates near 40°/s, Huygens must have been swinging some 5–10% of the time with swing rates of more than six times above the design limit.

It is interesting to note that the purpose of the tilts between the three slits was to infer the apparent solar zenith angle and thus the tilt of Huygens toward the Sun, assuming that swing speeds were small and thus the slit crossing speed could be calculated from the rotational rate of Huygens. Based on that assumption, we inferred typical tilts of Huygens of more than 20° during the initial analysis within days of the descent. By putting all our data sets together, however, it became very clear that the tilts of Huygens were much smaller, and that the large variation of slit crossing times must have been due to high swing rates. One can almost assume negligible tilts and calculate the swing rate for each Sun Sensor observation, just the opposite way as it was intended.

7.5. Data of error events

The Sun Sensor software was capable to distinguish real pulses from noise spikes observed in tests. For real pulses, the three pulses of the three slit crossings should roughly be spaced similarly, the widths of the pulses should be similar, the recorded intensity should be in the expected range, the timing of the central pulse should roughly be as expected based on the extrapolation of the previous two central pulses, among other constraints. Among some inferred 700 detected pulses, 28 were identified on-board as being outside the expected range, and the timing and reason was transmitted each time as one of about 12 error codes. In each case, the Sun Sensor went out of lock, which means that it lost the knowledge of the rotational state of Huygens. It then waited for consistent signals for three consecutive rotations and went into lock again, as expected. We now make use of the data of the error events.

While Fig. 11 displays data for a phase of the swing yielding extreme values, a more realistic approach considers all possible values of the phase. We tried to simulate the performance of the Sun Sensor in a statistical sense with a Monte Carlo calculation. For each rotation, we randomly selected a phase of the swing between 0° and 360°, and we randomly selected a swing rate based on an assumed exponential probability distribution with a constant average. For each simulation, we counted the encountered error events of the Sun Sensor for each of the 12 possible error codes. Then, we ran the simulation 100 times with different starting values of the random number generator. Note that the only adjustable parameter in this simulation was the average swing rate. Average swing rates below 10°/s and above 15°/s could not retrieve the actual performance of the Sun Sensor. With an average swing rate of 13°/s, the fit became very good. The fit became even a little better if we allowed the average amplitude to slowly change throughout the descent. While this may have been true, our data alone is not sufficient to make such a claim. For an average swing rate of 13°/s, we find the following frequency of error codes: 17 times actually (17 times in the simulation) the central pulse did not occur near the middle of the slit crossing time; 4 times actually (twice in the simulation) the timing of the fourth pulse, expected almost one rotation later, came too close after the third pulse, indicating a triple crossing of the same slit; three times (once) the widths of pulses varied too much; once (zero times) the fifth pulse came too early. All the remaining error codes never happened actually, and also never in the simulation. This is perfect agreement within the statistical variations from one to the next simulation, except for one error code, the case of three observed cases versus one in the simulation, where the widths of pulses varies too much.

We have a simple explanation for this case. Our simulation assumed constant slit widths, where the width of a pulse only depends on the slit crossing speed, the component of the speed vector perpendicular to the slit. However, in our laboratory calibration tests we determined that the very ends of the slits are out of focus, and that slit crossings near the ends produce wider pulses. In the cases shown in Fig. 10, the Sun does not come close to the ends of the slits. This would only happen if Huygens were tilted some 10° in the direction to decrease the apparent solar zenith angle. This actually happened between MT 1600 and 1800 (72–65 km altitude), right after Huygens reached the layer of minimum wind speed, and the accelerating wind caused Huygens to tilt in this direction. One of the three observed cases occurred in this interval, which makes the fit close to perfect even for this error code.

From the good agreement in the distribution of error codes between the observations and the simulations, we conclude that the performance of the Sun Sensor is well understood by an average swing rate of Huygens near 13°/s. For a harmonic oscillation of 1.2 s period, this corresponds to 2.5° swing amplitude. If the swing was more complex, the swing rate would be similar, but the swing amplitude could be different. The swing rate probably varied strongly, possibly even on short time scales, and reached above 40°/s some 5–10% of the time. This statement corresponds to the altitude range of 110–30 km. At low altitudes, the average swing rate was closer to 5°/s (1° swing amplitude), sometimes reaching 8°/s, as implied by smeared exposures (Section 2.1).

A swing of 1° amplitude requires a torque of about 10 N m, which seems possible simply by considering the probe size of 1.3 m and the drag force on the probe of 60 N in combination with some asymmetry of the drag due to

turbulence. The highest recorded swing amplitudes eight times as much seem more difficult to explain. This needs to be addressed in further investigations.

In retrospect, one could have designed the software of the Sun Sensor so it would handle high swing rates better, although correctly dealing with a "looping" Sun would be difficult. Even if it could be done, the unstable rotational rate of Huygens did not allow predicting the azimuth one rotation ahead. Even if that were solved, the direction of the probe's rotation opposite as intended would have been detrimental to some measurements; they always would have been taken at a direction where they Sun caused saturation instead of random directions providing useful, unsaturated data.

8. The geometry after landing

8.1. Altitude of the DISR camera

The window of the SLI camera was 45 cm above the bottom of Huygens, excluding the small Surface Science Package (SSP) penetrometer (Zarnecki et al., 2005) below the foredome. Considering that Huygens decelerated for about 12 cm upon impact (Zarnecki et al., 2005), the rest altitude of the SLI window should have been about 33 cm above the ground level, if the ground were flat. Images taken after landing suggest that most of the area near the landing site is quite flat, except for some rocks. If first contact occurred with a rock, the rest altitude could be higher. Initially, we estimated all distances and rock sizes on an assumed SLI altitude of 35 cm, but noted that all these numbers scale with the SLI altitude (Tomasko et al., 2005). Here we use three methods to better constrain that number.

The first method uses the parallax between the MRI and HRI cameras. The windows of the MRI and HRI are displaced by 24 ± 0.5 mm according to the design. At a distance of 35 cm, this gives a parallax of about 4°. Since we calibrated the geometry to 0.03°, and since we can identify a few features simultaneously in MRI and HRI frames taken after landing, we can determine the distance of the ground to 2% accuracy. The accuracy is limited mostly by the uncertainty in the displacement. We find that the SLI window was 48 ± 2 cm above the ground.

The second method uses the sharpness of features in the HRI images. Based on our analysis of the PSFs measured in the laboratory (cf. Section 2.3), we have an estimate of the optical aberrations of the HRI system, particularly the field curvature. We then generated PSFs for point sources at distances between 30 and 60 cm. These PSFs look like disks with a hole in the center due to the central obstruction, and the apparent diameters of the disks is roughly inversely proportional to the distance of the source, although the actual diameters of the disks are always similar to the diameter of the field lens of the HRI, which is 8 mm. We found nine features in the HRI images which look like such disks. They probably originate from small bright grains on a generally darker ground. For each feature, we measured the best fitting PSF and thus the distance of the feature. We found an altitude of the SLI window of 44 ± 3 cm above the ground, where the error bar derives from the scatter of the nine data points. In reality, the features on the ground are not point sources, so that part of the widths of the disks is due to the finite sizes of the features. Therefore, the number of 44 cm is a lower limit on the altitude. Nevertheless, considering that the central obstruction was mostly visible and that the edges of the disks appeared quite sharp, we estimate that the effect of the finite sizes of features was minor, and that the actual altitude was only a few cm more than 44 cm.

The third method uses the parallax between the MRI and the Surface Science Lamp, which are displaced by about 10 cm, but point in similar directions. We made laboratory measurements with our spare instrument, assuming that it is similar to the flight instrument. We took images of a white sheet at various distances illuminated by the lamp and compared the recorded intensity contours with those seen in the Titan images after landing. We found an agreement in the displacement of contours for altitudes of the SLI window of 48 ± 3 cm.

Considering the agreement of all three methods, we conclude an altitude of the SLI window of 48 ± 2 cm above the ground probed by the MRI and HRI images, where the ground seems flat and there are no large rocks. The center of the probe was about 2 cm closer to the ground based on the tilt discussed later. Considering the 45 cm nominal altitude difference between the bottom of the probe and the SLI window, our measurement of 48 ± 2 cm, and the 2 cm tilt, we conclude that the bottom of the probe rested at an altitude of 1 ± 2 cm above the ground level. Considering the deceleration distance of 12 cm, the first deceleration must have occurred 13 ± 2 cm above the ground level seen in HRI and MRI images, possibly by touching a rock or some elevated terrain. This seems quite possible since several of the rocks visible next to the probe rise about 15 cm above the main ground level. Also, the visible terrain looks flat, but it could be tilted below the probe and to some degree even in the imaged regions. Note that Tomasko et al. (2005) stated that the surface height was assumed to be 35 cm, and all distances and sizes of features in the surface image were based on this number. Thus, these distances and sizes need to be increased by 40% to account for the revised height of 48 cm.

A completely independent measurement of the height of Huygens at the surface was performed by Pérez-Ayúcar et al. (2006) through an analysis of interference of the radio transmitter beam with the beam reflected from the surface as Cassini approached the horizon. They derived an effective height of 75 ± 5 cm for the radio transmitter. The geometrical center of the 20-cm long transmitter is 72 cm above the bottom of Huygens, but the phase center is estimated to be 2 cm higher, which is 74 cm above the bottom of the probe (Pérez-Ayúcar, private communication). This puts the bottom of the probe at 1 ± 5 cm above

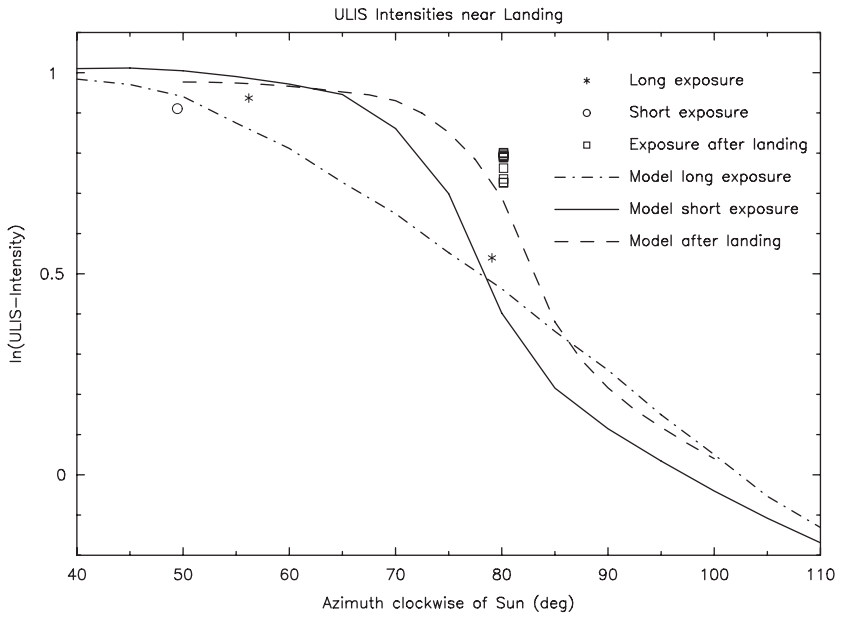

Fig. 12. A magnified section of Fig. 9, but with the inclusion of the measured ULIS intensities during the first 20 s after landing (open squares near 80° relative azimuth). The dashed curve is the expected intensity for the determined tilt of Huygens after landing. The open squares are placed near 80° relative azimuth, based on a rotation function extrapolated to the landing time. They fit the dashed line if shifted to 78° azimuth, the adopted value.

ground level, in good agreement with our result of 1 ± 2 cm above ground level.

8.2. Azimuth of DISR after landing

The AGC gain data and several ULIS exposures taken during the last minute of the descent constrain the azimuths during that period. If one extrapolates this to the time of landing, one finds an azimuth of the Huygens z-axis, the center of the DISR viewing direction, between south and SSW, and probably closer to the middle of this interval. The most accurate determination of the azimuth after landing, however, comes from ULIS exposures taken from the ground. The ULIS rotation function has generally moderate gradients, but for a section of about 30° just west of south, the gradient is very steep due to the Sun disappearing at the edge of the field of view. Luckily, Huygens came to rest just within this interval. A comparison of the rotation function with the actual data, before and after landing allows us to constrain the resting azimuth (Huygens z-axis) to $193 \pm 5°$, which is 13° west of south, or 78° to the right of the solar azimuth (Fig. 12).

8.3. Attitude of Huygens after landing

The best constraint from DISR about the rest attitude comes from the comparison of the sky brightness in SLI images taken before and after landing at similar azimuths, taking into account the gradual decrease of brightness with altitude. This yields a pitch after landing of $-3 \pm 1°$ and a roll within a few degrees of zero.

More accurate are measurements by the SSP tilt sensors (Lorenz, private communication). Since there are concerns that one of the tilt sensors may have had a constant offset, we will only use relative tilt data here. For the last 20 SLI exposures, we measured an average pitch of 0.3° and an average roll of −0.3°. These data are the most reliable because of the visibility of the horizon in these images. The average SSP tilt data for these 20 instances are 0.3° for TIL-X and −7.6° for TIL-Y (Lorenz, private communication). Considering the directions of the tilt sensors, we used this relationship between pitch/roll and SSP tilt data to convert the SSP tilt data measured after landing, which are 2.0° for TIL-X and −8.6° for TIL-Y, into pitch of −3.1° and roll of 0.9°. This means DISR is 3.1° looking up and 0.9° rotated clockwise in the viewing direction. These data are estimated to be accurate to about 0.5°. They are consistent with the data using the sky brightness. In other words, SSP detected a change of average tilt of 3° at impact, which corresponds to a decrease of pitch of 3° and an increase of roll of 1°. Since pitch and roll averaged near zero before landing according to our investigation, they must have been −3° and 1°, respectively, after landing.

Because the horizon on SLI images after landing seems to be depressed by 1.5°, and because the pitch was −3.1°, the horizon was actually raised about 1.6°, which indicates moderate relief south of the landing site. Because the horizon in SLI images after landing does not seem to be tilted either way, but the roll was 0.9°, the horizon actually was sloping up toward the left by about 0.9°, a very gentle slope. Images taken before landing suggest higher hills to the east and lower hills to the west, simply judging from the contrast of features, which is consistent with such a slope.

8.4. Motion of Huygens after landing

During the 70 min after landing, while Cassini still was above the horizon and received data, we received about one image per minute for each of our three imagers. While some of the MRI and HRI images were saturated near the lamp spot, we compared all non-saturated sections of all three imagers as function of time. For the SLI images, we found all features moving down by a constant rate of 0.08°/h. The precision was 0.01°/h based on the scatter of positions from image to image. The horizontal motion was 10 times smaller and not significant. We also checked for a rotation around the center of the image and found none within the measurement precision. We also checked for motions due to translational movements of the DISR camera, particularly a possible sinking, but we found none above our measurement threshold of 2 mm/h.

We then did the same investigation for the MRI images. We found that features moved up at 0.05°/h to a precision of 0.01°/h, but no other motions. The HRI images did not allow an accurate measurement. Our conclusion is that the DISR camera did not move much during these 70 min, but that Huygens tilted by about 0.06°/h. This corresponds to a sinking of the opposite side of Huygens at about 1 mm/h. In the central part, where Huygens touched the surface, the sinking speed was half as much. Note, however, that an additional motion of the whole probe at constant orientation is possible up to 2 mm/h, as discussed in the previous paragraph. The sinking could have been caused by constant evaporation of methane just below Huygens due to the heat flow from Huygens, which was sufficient to evaporate a few mm of methane (Lorenz, 2006). The tilting may have been caused by the ground being harder on the DISR side than on the opposite side. Note that Huygens was tilted 3° on the ground, but typically only 1–2° during the final part of the descent. Thus, the tilting probably occurred on impact, possibly due to a large rock on the DISR side of Huygens, consistent with this being the "harder" side.

The rates measured from SLI and MRI images do not agree as well as expected. It is possible that the changing temperature structure of the optics caused small motions, for example between the lenses and the fiber optics, which made the features appear to move. We estimate those apparent motions to be about 0.02°/h, which can explain the slight discrepancy between the SLI and MRI data. We estimate that the observed 0.06°/h is probably real, but we cannot completely rule out that this motion is only apparent. Motions between the optical elements depended on the temperature structure within DISR, and the temperature structure after landing may have been very different from those encountered during laboratory tests.

For comparison, the SSP tilt sensors recorded a motion of Huygens on the surface in the same direction, but with a larger speed of 0.2°/h (Zarnecki et al., 2005).

8.5. Terrain near the landing site

We now try to connect features seen in images before and after landing, although this is speculative due to the large differences in pixel scale. The images after landing looked at a central azimuth of 193°. The last frame before landing with a matching azimuth was HRI frame 716. It was taken 59 s before landing from 270 m altitude, and the probe did exactly one more full rotation until impact. The direction of motion during this final descent minute was probably to SSE according to our low altitude data, while the speed was constrained by data from Bird et al. (2005).

With this assumption, Huygens landed close to the lower left edge of the frame 716. This means that the right half of the images taken after landing probably overlap with the left part of frame 716. According to frame 716, the area in front of the landing site was almost featureless dark up to two bright stripes aligned east–west, some 30 and 35 m from the suspected landing site. Note that the largest rocks of some 20 cm diameter seen on the ground are smaller than the pixel size of 30 cm in frame 716, or the PSF size of 50 cm. Thus, these rocks are not expected to be visible, although some mottling seen in the dark area in frame 716 close to the noise level could come from some of the rocks.

Since bright features appear to correlate with higher areas, the bright streaks in frame 716 could be hills seen from the surface. These hills are then almost 1 m high and some 3 m wide. Other bright features are much further away from the landing site. Unless they are much higher hills, they would not be visible from the landing site. The next major bright feature at 150 m distance would need to be more than 4 m high to be visible which is possible, although it does not seem to be more pronounced than the closer ridge as imaged during the late descent. A further, similar feature at 600 m distance is probably less than 16 m high and thus hidden.

In the SLI images of the landing site (ref. Fig. 13), the apparently flat area with rocks may extend to about 30 m distance, where the rocky area turns into an area without small features. This transition may be the transition from flat terrain to the relatively steep slope climbing almost 1 m across 1–2 m distance. If the furthest rocks visible are at a distance of 30 m, they are just about the same size as the rocks seen in the foreground. In the left part of the images taken from the surface, there is a bright, horizontal line between the end of the rocky area and the horizon. This could be the closer hill, while the horizon marks the further hill, some 5 m further away. These are our best guesses, while other guesses may be equally valid.

8.6. Variable distortion

The 82 SLI images after landing match each other geometrically on small scales, within about 10°, but not on larger scales. Different parts of the images seem to be shifted randomly in different directions by up to about half a pixel, or 0.1°. Typical displacements are more like a

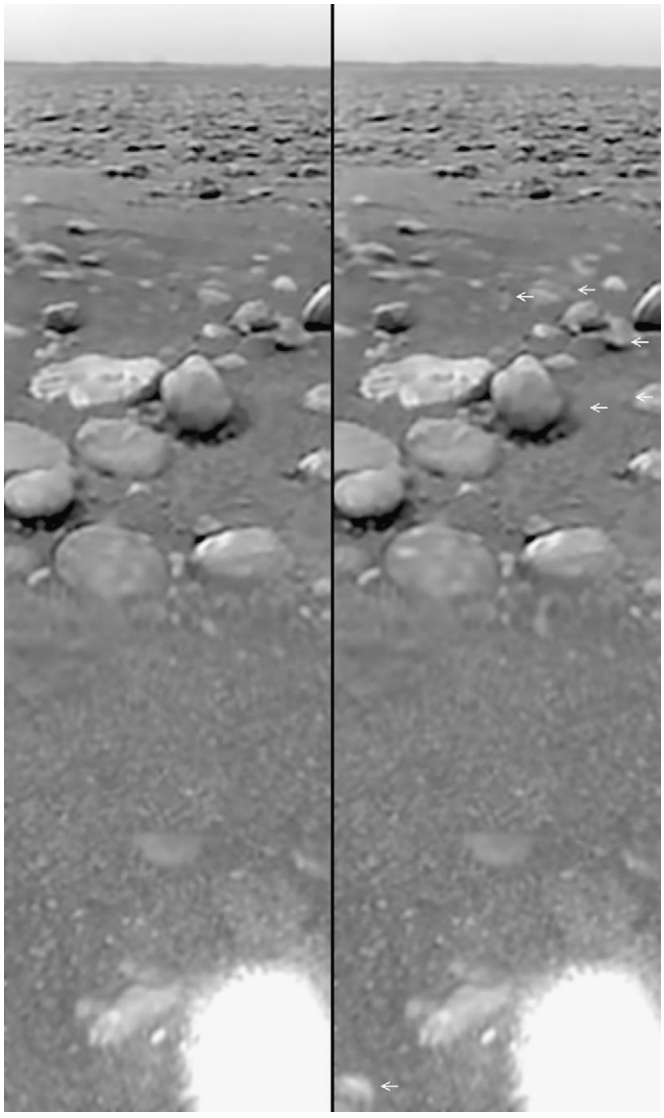

Fig. 13. The average of all SLI and MRI images taken after landing (left) and a version of the same view, where near each of six arrowed regions only one selected image was used, the image which contained a bright feature.

couple of arc-minutes. Our best explanation is that our lamp was warming the surface, which caused warm air bubbles rising in front of the imagers. Note that our lamp put a similar amount of radiation on the illuminated spot as the high Sun warming dark surfaces on Earth. Also, a parcel of air with a 1 K temperature difference with respect to the surrounding air causes refraction of light to be some 15 times larger than for a similar parcel on Earth, since Titan's air density is five times as large, while its temperature is three times lower. We have not done any modeling of refraction to check if our explanation is reasonable.

8.7. Variable features

Whenever we imaged the same surface area twice during the descent, we saw the same features, except for limitations due to resolution or contrast. On the other hand, for the about 80 images of each imager after landing, this is only true for most of them, while about six of them have a bright feature at random locations (Fig. 13). These features look different from artifacts such as cosmic ray hits, so they may be real. In principle, one could attribute five of them to very unusual cosmic ray events, but this is not a feasible explanation for the well resolved one in the lower left corner of Fig. 13. They cannot be closer than about 30 cm to the cameras, because they look almost as well in focus as the ground. All of them appear where the ground is closer than 3 m distance; none of them appear in the sky or in the upper part of the SLI. This makes it likely that they are much closer to the ground than the 48 cm height of the cameras. If they are near the surface, they are all about 2 cm in size. They appear on flat areas as well as ice-rocks. This may argue against a variable effect on the surface, such as a temporary methane bubble evaporating as the surface got warmed by Huygens.

They could be something light-weight carried across the surface by the light wind. For reasonable wind speeds (~0.1 m/s, Lorenz, 2006), exposure times were short enough that moving objects would not have been smeared; yet the time between successive exposures was long enough to move objects much further than the diameter of the observed region. About 1/200,000 of the Titan's surface would need to be covered by these objects, at least near the landing site, or about one object for every 50 m^2.

Another possible interpretation of these features is splashing raindrops hitting the surface. The contrast in the splashes would need to be different from that of splashes on Earth. One would need an explanation why no significant cloud was detected where methane was supposed to condense into raindrops. According to Lorenz (1993), such raindrops would evaporate before hitting the surface. However, Graves and McKay (private communication) recently expanded Lorenz' model of pure methane raindrops to mixtures of methane, ethane, and nitrogen, and they found that raindrops of at least 2–3 mm radius forming between 7 and 15 km altitude would make it to the ground. Using these sizes and the rainfall estimate of 10–100 mm/year by Tokano et al. (2006), we calculated the frequency of raindrops hitting the surface and concluded that splashes would need to last some 200–2000 s in order to match the observed frequency. However, images taken in 10–20 s intervals show that the visible splashes cannot last longer than 20 s. One may solve this discrepancy by proposing much higher rainfall rates than Tokano's. However, even Tokano's rainfall rate would probably clear out the aerosols in the lower atmosphere faster than they can be replenished. One could argue that the visible haze in the lower atmosphere is indeed rain and not aerosols, but then a rainbow should have been clearly visible, but none was detected. Thus, this rough estimation above argues against the idea of raindrop splashes, but in view of the uncertainties of all parameters above, and the

lack of another good explanation, this possibility may still be promising. A more detailed study is warranted.

As we improve our understanding of the processes on Titan's surface over the coming years, we may get better ideas, what the observed features may be. If they are real, the closest one, in the lower left corner of Fig. 13, reveals the most structural features.

9. Surface wind

Huygens landed on the surface with DISR looking roughly south, as discussed in the previous section. The last measurements of the trajectory from DISR indicate wind directions to the south–east. Thus, the parachute probably moved into the 170°-wide fields of view of the spectrometers right after landing. In fact, the ULIS took data during the seconds after landing. While dozens of spectra taken later than 20 s after landing recorded constant intensities within 0.5% rms, the five exposures within 20 s after landing show a significant drop of intensities at all wavelengths of up to 6%, a likely signature of the parachute obstruction of the sky.

We tested if we could match the observed light curve with a model calculation. The shape and motion of a parachute after the load is gone is hard to predict. Here, we simply try some more or less plausible possibilities (Lorenz, private communication). We assume that the parachute was still spherical. In the nominal case, the parachute has its previous diameter of 1.97 m. We also considered two cases with a 1.5 times larger projected surface area, a possible flattening, and a 1.5 times smaller projected surface area, a possible partial collapse. The expected sinking speeds are 0.5 m/s for the nominal case and 0.4 and 0.6 m/s, respectively, for the other cases, based on a mass of 0.7 kg and a drag coefficient of 0.45 (Lorenz, private communication). We also considered that the parachute may fall about 1 m after the impact of Huygens with the original speed before it slowed to the terminal speed after landing. We used our sky intensity model for 938 nm wavelength to predict data numbers for the ULIS as function of time. The parachute was non-transparent and close to fully reflective. We varied the wind speed and wind direction to find fits with the observed light curve. Lorenz (private communication) also considered a 30% decrease of the falling speed after 5 m of descent due to the off-loading of the swivel of mass 0.4 kg. We did not include this extra sophistication in our calculations because the sensitivity of the ULIS is low near the horizon, where the speed change would make the largest displacement.

For the nominal case (0.5 m/s sinking speed), we find a fit good to 0.5% in intensity for a wind speed of 0.3 m/s and a wind direction towards azimuth 160° (20° east of south, cf. Fig. 14). For the other two cases the fit is only slightly worse with the same azimuth and slightly different speed. Considering uncertainties including those about the parachute shape, we find a wind speed of 0.3 ± 0.1 m/s and an azimuth of $160 \pm 10°$. This is similar to the latest DWE data, indicating a wind component of about 0.4 m/s toward ESE. Note that an azimuth above 165° or 170° should have shown the parachute in the SLI images taken after landing which was not the case. Also, an azimuth below 140° would have obstructed the Sun causing a very large drop in intensity which was not observed either.

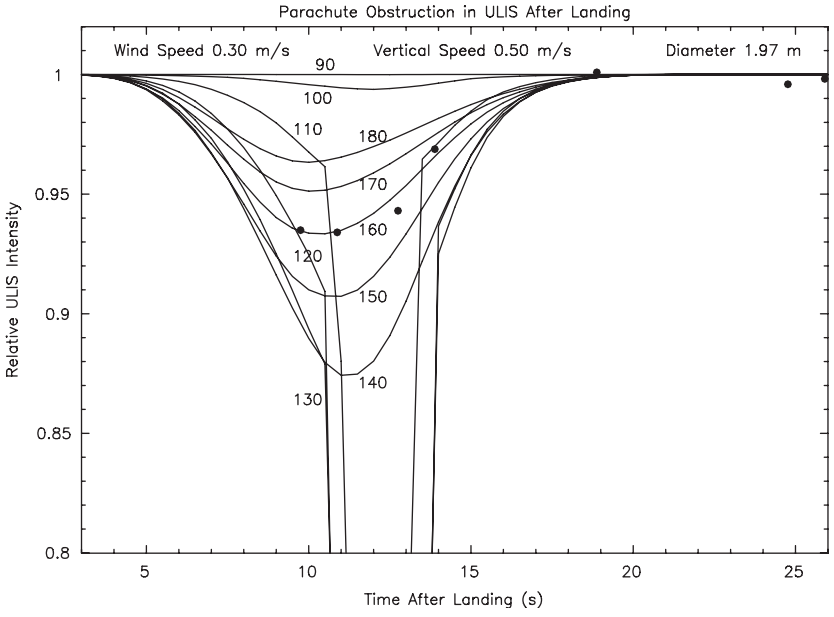

Fig. 14. The light curve observed with the ULIS shortly after landing. The model light curves are calculated for azimuths of the wind vector every 10° between 90° (toward east) and 180° (toward south). The three interrupted curves (110–130° azimuth) indicate an occultation of the Sun by the parachute, which was not observed. The curve for a wind direction 160° fits the data points to 0.5% rms, which is the scatter for data points later than 19 s after landing.

Our wind speed range of 0.3 ± 0.1 m/s overlaps with the upper limit of 0.25 m/s determined by post-impact cooling (Lorenz, 2006). Both results are even more consistent with each other if one considers that the parachute-derived wind speed corresponds to the layer of about 10 m above the surface, while the cooling-derived wind speed corresponds to the layer of less than 1 m above the surface, where the wind speed may be lower.

10. Discussion

10.1. Trajectory

The main component of the motion of Huygens, the zonal component, was captured by the DWE (Bird et al., 2005). DISR data are consistent with this determination, but mostly less accurate. Only in two sections, where DWE took no data and assumed linear interpolation, did DISR data contribute a slight correction of the zonal motion.

The meridional motion is constrained by our analysis. Huygens moved about 2° north of east on average from the release of the first parachute to an altitude of about 50 km. During this period, we only know the total (or average) meridional motion. Then, the motion of Huygens turned slightly to the right up to about 5° south of east between 30 and 20 km altitude (Fig. 15). At 12 km altitude, where the direction moved back to eastward, Huygens passed almost over the landing site, only slightly to the south of it (Fig. 16). It continued to move to the east but continuously decelerating, until it reversed motion between 6 and 7 km altitude. From 6 to 1 km altitude, it moved to the ENE, passing by the landing site again, but this time to the north (Fig. 17). Then it turned to the left through almost 180° with the descent below 0.7 km altitude toward SE or SSE. Between 250 and 10 m altitude, the meridional motion of Huygens is not constrained by observations, but we determined that the wind moved the parachute to the SSE after landing. Since our data are the only available data on the meridional motion of Huygens during the descent, the latitude variation of Huygens for DTWG analysis (Kazeminejad et al., 2007) was directly taken from our study.

While our zonal motion of the trajectory is derived from DISR imaging, DTWG work (Kazeminejad et al., 2007) did not use our data for their zonal motion but based their reconstruction on the DWE zonal wind measurements from Bird et al. (2005). As shown in Fig. 18, the difference down to 12 km altitude is within our accuracy. However, below 12 km altitude, their trajectory is inconsistent with DISR imaging. Between 12 and 5 km altitude, they used interpolation to define the zonal motion due to lack of DWE data. Further down, another interval without DWE data could also be improved very slightly. In the dashed curve of Fig. 18, we indicate how we modify their trajectory for these two intervals in order to be consistent with our constraints. Table 4 lists the westward longitude shift for this modification, with linear interpolation assumed between the data. We adopt the shifted trajectory here, and the data given in Table 1 are calculated with that trajectory.

Otherwise, there is good agreement between the zonal motions derived from DISR imaging and DWE. This has indirect implications that the altitudes we used are close to the truth. On the other hand, the radar altimeter indicated

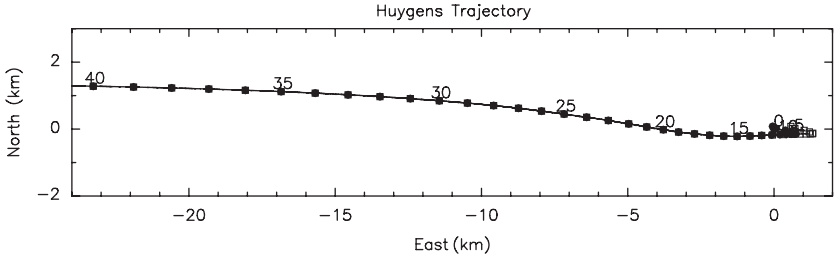

Fig. 15. The trajectory of Huygens with respect to the landing site, starting at 40 km altitude. The numbers indicate the altitude in km. Solid dots indicate the position of Huygens every full kilometer of altitude.

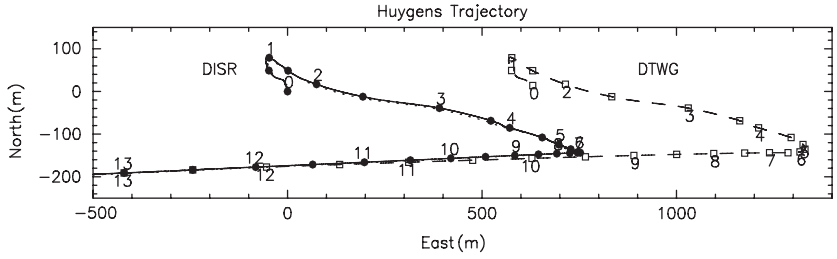

Fig. 16. The trajectory of Huygens, similar to Fig. 15, but starting at 13 km altitude. The DTWG trajectory (cf. Appendix A, DTWG#4) goes further east than the DISR trajectory and is inconsistent with DISR imaging data. Solid and open circles indicate the position every 500 m of altitude. Irregularities such as the slow motion between 4 and 3.5 km altitude are real.

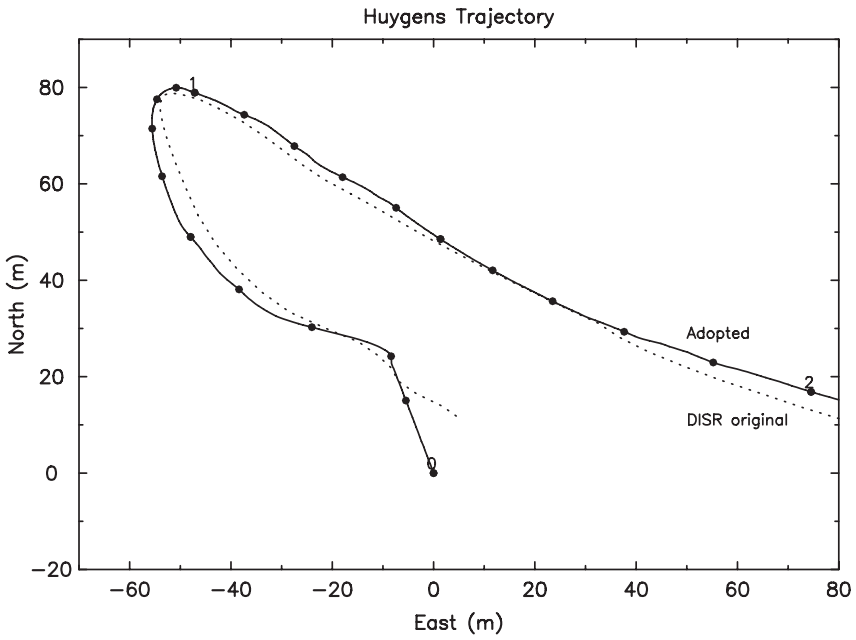

Fig. 17. The trajectory of Huygens starting at 2 km altitude. Solid dots mark the trajectory every 100 m of altitude. The difference between the original (dotted line) and the adopted (solid line) trajectories is within the accuracy of the data. The direction of motion below 250 m altitude is not constrained, but the solid curve is consistent with the wind speed measured at landing.

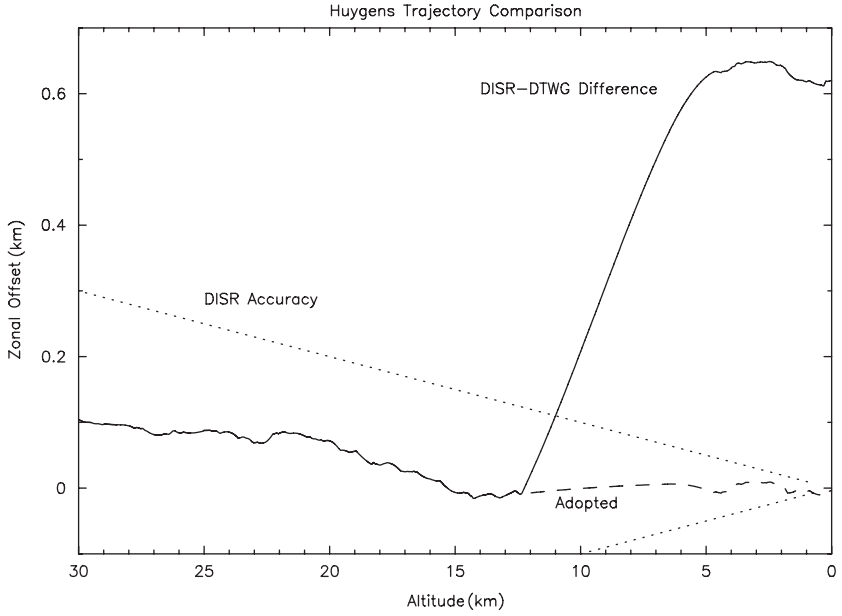

Fig. 18. Comparison between the DISR and DTWG trajectories in the zonal direction. A positive offset means that the position according to DISR is to the west of the position according to DTWG. Since the DISR data provided only relative positions, it was calibrated to the DTWG position at 15 km altitude. Above 12 km altitude, the zonal difference between both data is well within the DISR accuracy, but not below 12 km. The modification of the DTWG data suggested here below 12 km yields the adopted, dashed curve, which is consistent with our data.

altitudes some 6% larger (Trautner, private communication), which would give very different zonal motion for DISR imaging versus DWE, because the Doppler data was more sensitive to vertical speed than to horizontal speed. Below 3 km altitude, where DISR imaging constraints are quite tight, the discrepancy between DISR and DWE would be at least five times as large as the accuracy. Thus, altitudes in the lower 3 km cannot be off by more than 2%, and the radar altitudes can be rejected. DTWG (Kazeminejad et al., 2007) came to the same conclusion based on a more thorough analysis with more data sets, but not including the observation stated here.

We also suggest another, much smaller change for the last 35 s of the descent. The trajectory of Kazeminejad et al. (2007) followed the ESE-motion of our preliminary trajectory ("DISR original" in Fig. 17), before we investigated

Table 4
Westward longitude correction to DTWG#4 of May 2006

MT (MT+)	0	10	20	30	40	50	60	70	80	90
6400	0.000000	0.000000	0.000000	0.000000	0.000000	0.000000	0.000000	0.000000	0.000102	0.000205
6500	0.000309	0.000414	0.000520	0.000626	0.000734	0.000842	0.000950	0.001060	0.001170	0.001281
6600	0.001393	0.001505	0.001618	0.001731	0.001845	0.001960	0.002075	0.002191	0.002307	0.002424
6700	0.002542	0.002659	0.002778	0.002896	0.003015	0.003135	0.003255	0.003375	0.003495	0.003616
6800	0.003737	0.003859	0.003980	0.004102	0.004225	0.004347	0.004469	0.004592	0.004715	0.004838
6900	0.004961	0.005084	0.005207	0.005331	0.005454	0.005577	0.005701	0.005824	0.005947	0.006070
7000	0.006193	0.006316	0.006439	0.006562	0.006684	0.006807	0.006929	0.007051	0.007173	0.007294
7100	0.007415	0.007536	0.007657	0.007777	0.007897	0.008017	0.008136	0.008255	0.008373	0.008491
7200	0.008608	0.008725	0.008842	0.008958	0.009073	0.009188	0.009302	0.009416	0.009529	0.009641
7300	0.009753	0.009864	0.009975	0.010084	0.010193	0.010301	0.010409	0.010515	0.010621	0.010726
7400	0.010830	0.010934	0.011036	0.011138	0.011238	0.011338	0.011437	0.011535	0.011631	0.011727
7500	0.011822	0.011915	0.012008	0.012099	0.012190	0.012279	0.012367	0.012454	0.012540	0.012624
7600	0.012708	0.012790	0.012871	0.012950	0.013028	0.013105	0.013181	0.013255	0.013328	0.013400
7700	0.013470	0.013538	0.013605	0.013671	0.013735	0.013798	0.013859	0.013919	0.013977	0.014033
7800	0.014088	0.014141	0.014193	0.014243	0.014291	0.014338	0.014383	0.014426	0.014467	0.014467
7900	0.014467	0.014467	0.014467	0.014467	0.014467	0.014467	0.014467	0.014467	0.014467	0.014467
8000	0.014467	0.014467	0.014467	0.014467	0.014467	0.014467	0.014467	0.014467	0.014467	0.014467
8100	0.014467	0.014467	0.014467	0.014467	0.014467	0.014467	0.014467	0.014467	0.014467	0.014467
8200	0.014467	0.014467	0.014467	0.014467	0.014467	0.014467	0.014467	0.014467	0.014467	0.014467
8300	0.014467	0.014467	0.014467	0.014467	0.014467	0.014467	0.014467	0.014467	0.014467	0.014467
8400	0.014467	0.014467	0.014467	0.014467	0.014467	0.014467	0.014467	0.014467	0.014467	0.014467
8500	0.014422	0.014377	0.014332	0.014286	0.014241	0.014196	0.014151	0.014105	0.014105	0.014105
8600	0.014105	0.014105	0.014105	0.014105	0.014105	0.014105	0.014105	0.014105	0.014105	0.014105
8700	0.014105	0.014105	0.014105	0.014105	0.014105	0.014105	0.014105	0.014105	0.014105	0.014105
8800	0.014105	0.014105	0.014105	0.014105	0.014105	0.014105	0.014105	0.014105		

Note: Entries are listed in degrees of western longitude.

Table 5
Trajectory adjustment near landing

MT	$\Delta\lambda$	$\Delta\phi$
8835 s	0.000000°	0.000000°
8840	0.000011	−0.000022
8845	0.000025	−0.000052
8850	0.000047	−0.000097
8855	0.000085	−0.000176
8860	0.000110	−0.000230
8865	0.000127	−0.000264
8869.77	0.000148	−0.000307

Note: MT, mission time; $\Delta\lambda$, adjustment for western longitude; $\Delta\phi$, adjustment for latitude.

the wind speed at landing. Since the wind speed at landing is toward SSE, and since there are no other constraints on the wind direction near the ground, the solid line in Fig. 17 for the last 200 m of the descent may be more likely than the dotted line. This small adjustment is listed in Table 5, with linear interpolation assumed between data, which would need to be applied in addition to the adjustment listed in Table 4. Again, the measured speeds from DWE are equally consistent with both trajectories.

10.2. Rotation

We used several components of DISR and the AGC gain structure to define the azimuth as a function of time throughout the descent (Table 3). Independent constraints gave consistent results. For example, relative azimuths for images based on the mosaic agree with AGC-derived azimuths to 1.8° rms, while they are estimated to be accurate to 1° and 2°, respectively. Thus, the rotation of Huygens is pinned down to almost 1° at altitudes below 40 km, and probably not much inferior above 110 km. In between, the accuracy is expected to be somewhat inferior, because there are fewer constraints.

Huygens started its descent with 7.28 RPM counterclockwise (Kazeminejad et al., 2007), looking down on the probe from above. The rotational rate changed smoothly toward an equilibrium rate of 3 rotations clockwise for each descending km, while the expected equilibrium rate was a similar value, but counterclockwise. Near MT 542 (125 km altitude), the counterclockwise rotation changed into the clockwise rotation for the rest of the descent. After the parachute exchange at MT 900 (111 km altitude), the rotational rate accelerated as expected for the faster descent speed. However, this lasted only 40 s. At MT 940 (109 km altitude), Huygens received a large jolt breaking its accelerating rotation. For the rest of the descent, we identified some 100 accelerating and decelerating irregularities of various strengths (Fig. 19). This was unexpected and is still not fully understood. We suspect that turbulence generated by Huygens could have been the cause. The largest jolts had amplitudes of more than 90° of rotation, about two orders of magnitude larger than our accuracy of 1–2°. The rotational rate was also instable on long time

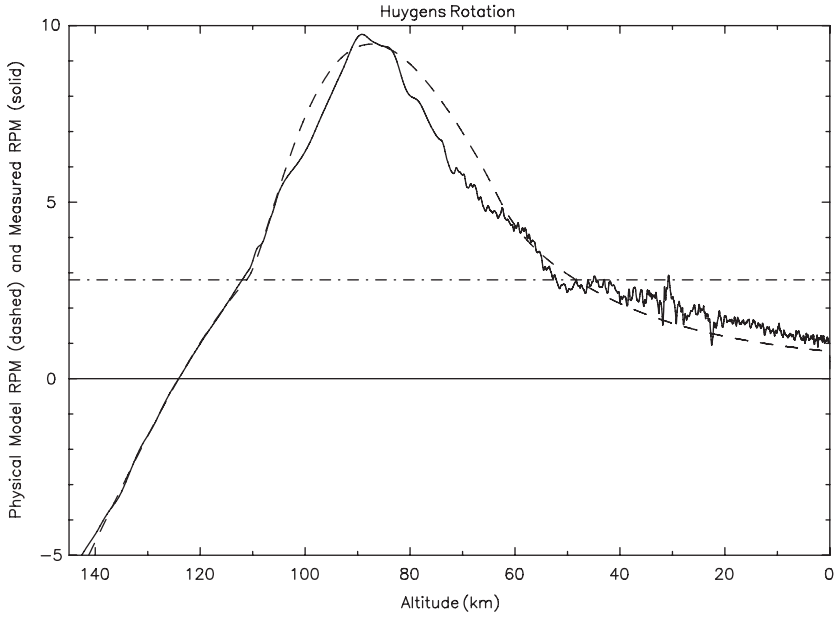

Fig. 19. The rotational rate of Huygens (solid line), compared to a model (dashed line), which has asymmetries of Huygens to impose a constant equilibrium rotation of 2.8 rotations for every km of descent (cf. horizontal dashed-dotted line). The fit is very close to perfect for the main parachute (above 110 km altitude), but worse afterwards.

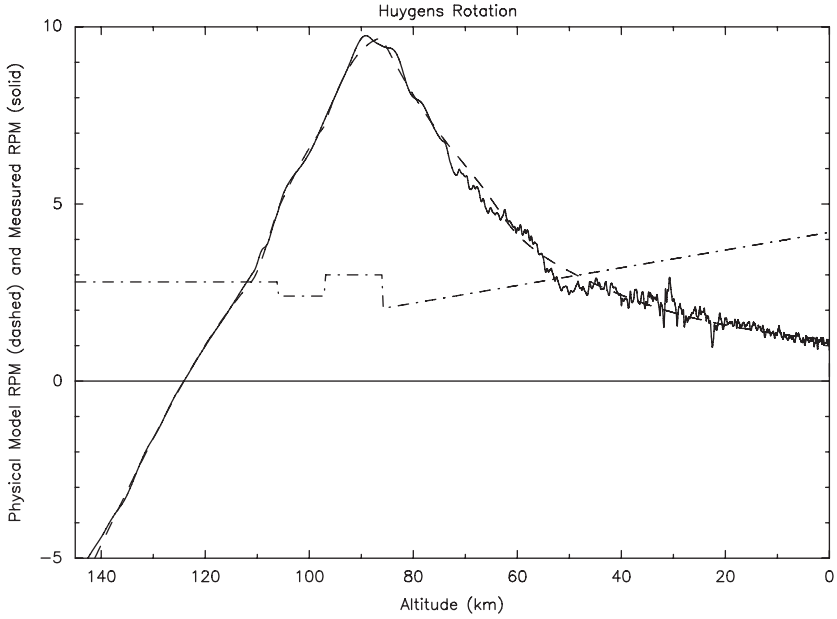

Fig. 20. Same as Fig. 19, but with the equilibrium rations per vertical km changing during the descent as indicated in the dashed-dotted line. Except for some unexplained high-frequency structure, the fit is much improved.

scales, where variable spin rates could be 'explained' by imposing a slowly variable equilibrium spin rate, which would correspond to something on Huygens changing shape or tilt during the descent (Fig. 20). After the parachute exchange, Huygens rotated on average going back and fourth between 2 and 4.5 rotations per descent km (Fig. 21).

The largest jolts visible in Fig. 22 correspond to torques applied to Huygens in the order of 0.1 N m, or forces in the order of 0.1 N if applied near the circumference of Huygens, which is about three orders of magnitude smaller than the total drag force on Huygens during the stabilizer phase. It did not take much to change the rotation of Huygens by a fraction of a RPM.

Fig. 22 may suggest that rotational accelerations became more and more frequent from 110 km altitude to the surface. However, this is partially due to the decreasing descent speed. As function of time, the accelerations were frequent throughout the descent on the stabilizer. Only the amplitudes decreased somewhat below 20 km altitude.

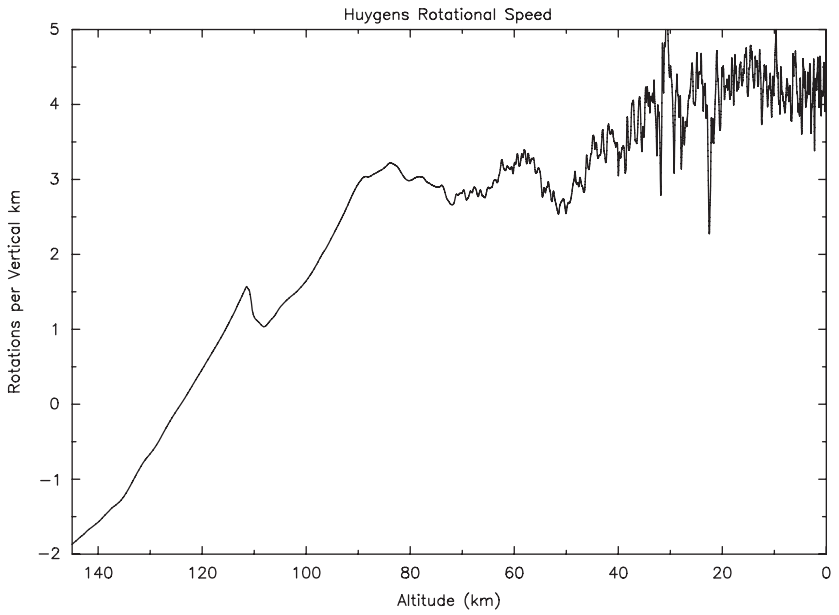

Fig. 21. The number of rotations per vertical km. Starting near 90 km altitude, the value was expected to stay constant, while the data show a lot of unexplained structure. All visible structure is real. Note, however, that possible high-frequency structure was not measurable where the descent speed was fast (70–110 km altitude).

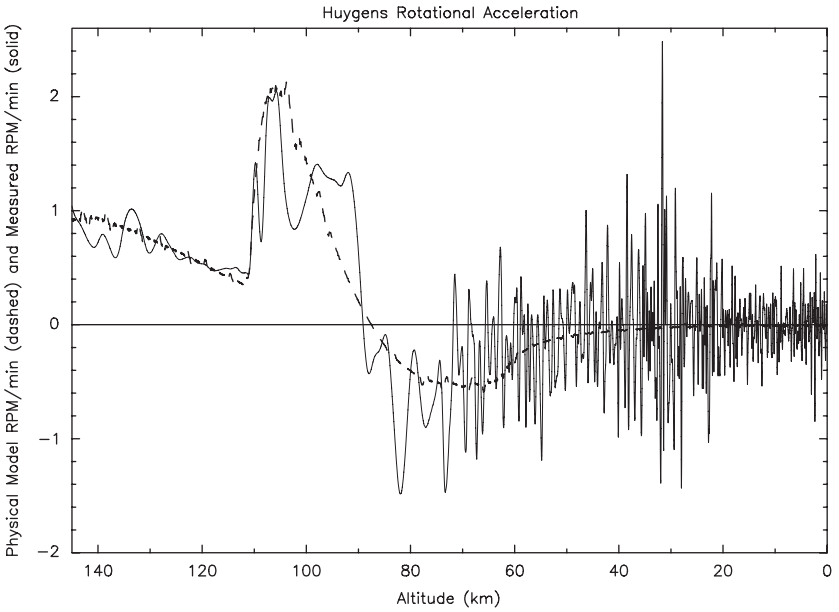

Fig. 22. The rotational acceleration of Huygens (thin solid line), compared to a model (dashed line). The data are close to the model for the main-parachute phase (above 110 km altitude), but less so afterwards.

Also, above 70 km altitude, the lack of structure in the AGC gain made it impossible to catch fine structure in the accelerations. On the other hand, above 110 km, the abundance of DISR data would have caught irregularities, and their lack is real. The rotation changed very smoothly while on the main parachute.

A major part of the design of the DISR data acquisition focused on measuring the rotational rate and then taking each of the thousands of exposures at predefined azimuths, assuming a smoothly varying rotational rate. Considering the real, unstable rotation after the deployment of the stabilizer (Fig. 22), there was no chance of obtaining exposures at predefined azimuths. DISR data were acquired at essentially random azimuths. This complicated our data analysis significantly. DISR was designed to provide a good rotational profile within a few hours of work, but it took many months. On the other hand, we expect that none of our scientific goals will be compromised due to the unstable rotation, and our results so far are as accurate as we could hope for with the expected rotation.

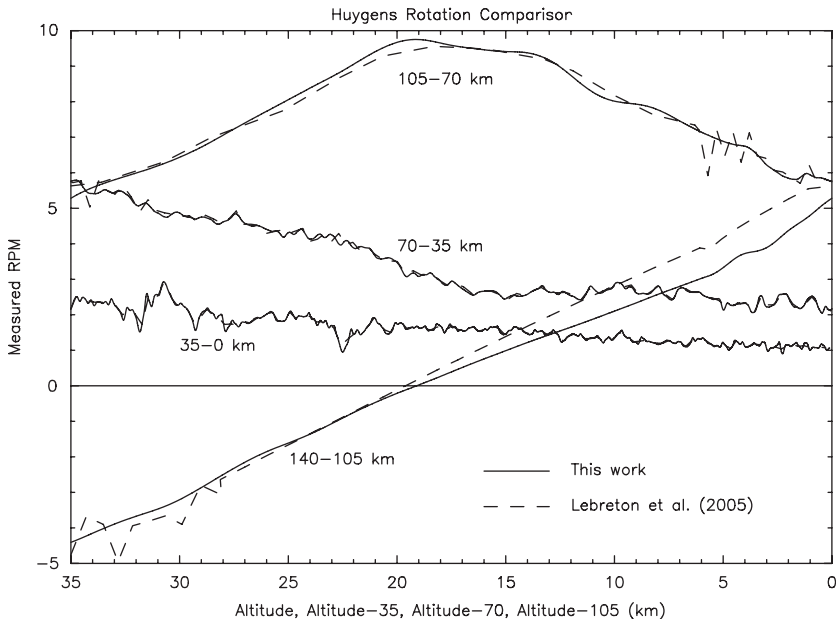

Fig. 23. The Huygens rotational rate determined here in comparison with Lebreton et al. (2005). The four altitude ranges are horizontally offset by 35 km in order to show small-scale features. Note the excellent agreement below 70 km altitude.

The rotation function was already determined by Lebreton et al. (2005) using the AGC and accelerometer data. Below 70 km altitude, there is excellent agreement between our and their determination (cf. Fig. 23). Above 70 km altitude, there are some differences, especially the 1 RPM offset between 120 and 105 km altitude. Above 70 km altitude, the AGC structure is so weak that we based our determination mostly on DISR data, and we are confident in our determination between 120 and 105 km. Also, their irregularities above 133 km altitude can easily be rejected with DISR data. On the other hand, their irregularities between 73 and 76 km altitude are hard to prove or disprove. The Lebreton et al. (2005) investigation of the rotational rate was done to three significant digits in order to show the general rotational rate. The purpose of our investigation was to preserve azimuthal accuracy of 1–2° over the course of 300 rotations, which required six significant digits (Table 3).

10.3. Attitude on long time scales and wind

As discussed in Section 3, the changing speed of Huygens must be caused by a tilt of the Huygens–parachute system (Fig. 24, Table 2). During the main-parachute phase, where accelerations were largest, we find a good correlation between measured tilts and the expected tilts based on the acceleration (Fig. 25). The difference of 2° rms between both tilts is consistent with estimated uncertainties. Thus, there is no indication of any deviation of the motion of Huygens and its parachute from the expected motion due to forcing of changing wind speeds.

Since the tilt of Fig. 24 is inferred by the difference of successive measurements of the speed of Huygens, one may suspect that the high-frequency oscillations of Fig. 24 may be due to noise in the wind measurements. However, if we slightly smooth the tilt data of Fig. 24, the observed correlation in Fig. 25 gets significantly worse. This indicates that the displayed high-frequency oscillations are real.

During the main-parachute phase, tilt measurements indicate that the mean tilt in the north–south direction was about 60% of the mean tilt in the east–west direction. Thus, wind variations occurred in both directions, the zonal and the meridional directions, although the magnitude was some 40% smaller in the meridional direction. This may not have been expected considering that the winds were mostly zonal. Our tilt data are not sufficiently closely spaced to retrieve profiles of acceleration or wind speeds. The DWE measured speeds in the direction WNW–ESE and then converted them to zonal speeds assuming no meridional speeds, which is not true on short time scales.

In order to retrieve a best estimate for the tilt in the east–west direction, we converted accelerations from the DWE into tilt where DWE had data, and we used our tilt data to fill in gaps of the DWE data as well as the spacing of our data points allowed it. On time scales above 1 s, the velocity vector of Huygens with respect to the atmosphere should be very close to the tilt of Huygens. If the parachute were not in the direction opposite to the velocity vector, it would adjust to this position within a fraction of a second. With the knowledge of the magnitude of the vertical speed and the direction of motion relative to the atmosphere, one can easily calculate the horizontal speed of Huygens with respect to the atmosphere (Fig. 26), which is the product of the vertical speed and the tangent of the tilt. This speed is up to 12 m/s in both directions and is the difference between the wind speed and the horizontal Huygens speed

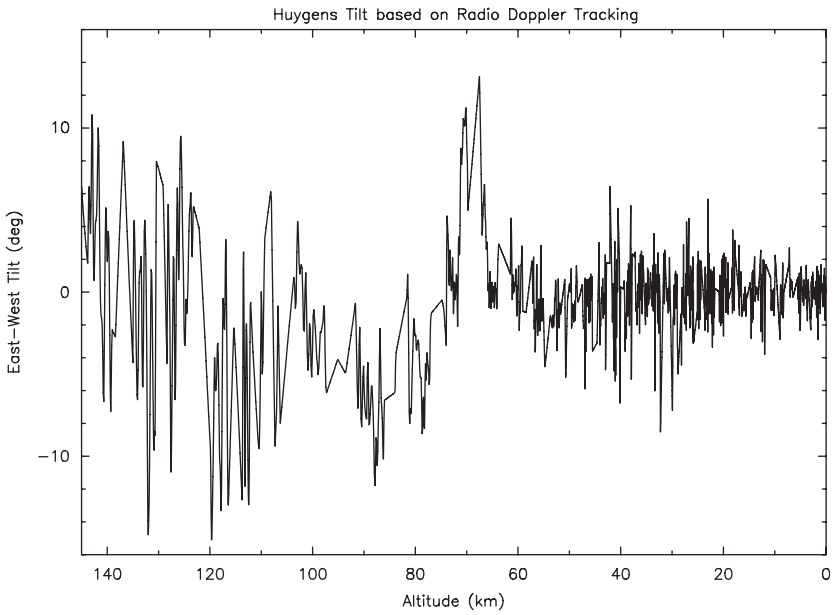

Fig. 24. The low-frequency component of the east–west tilt of Huygens as function of altitude. A positive tilt means that Huygens is to the west of the parachute.

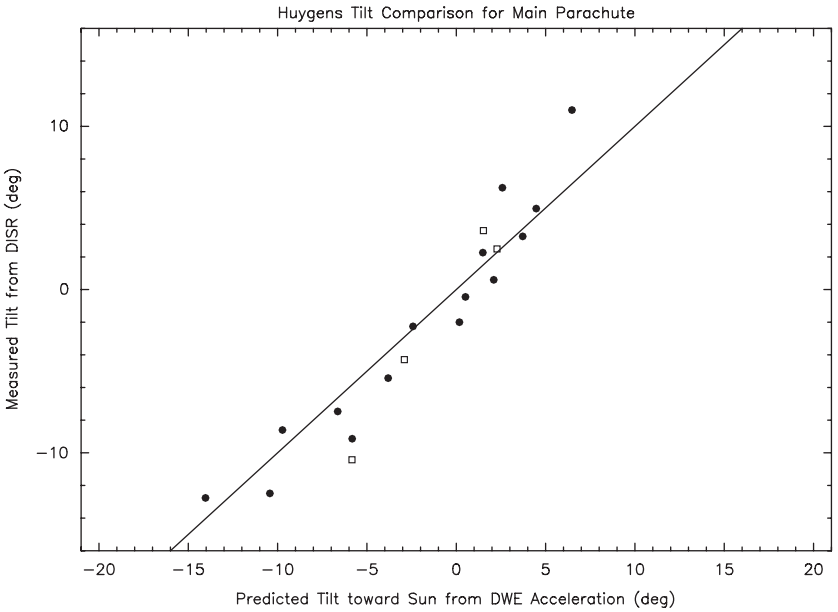

Fig. 25. Correlation between inferred tilt of Huygens based on DWE acceleration data and the observed tilt based on intensity contours measured in SLI images. Solid dots indicate full SLI images, while open squares indicate SLI strip data.

relative to the ground. Thus, speed measurements from DWE corresponding to the speed of Huygens can be converted into wind speeds and vice versa. Because of the up to 12 m/s difference between the wind speed and the Huygens speed, our nomenclature is different from some other investigations, such as Bird et al. (2005), who called the measured horizontal speed of Huygens the wind speed.

After the parachute exchange, the accelerations decreased more and more, while the tilts increased, and the correlation became weaker. About 900 s later, at altitudes near 70 km, the accelerations became very small and the correlation disappeared completely. Huygens did not swing any more as expected, since motions on short time scale became dominant.

Although tilt data of individual exposures differ by many degrees from the expected tilt based on wind variation data, once more than 10 data points are averaged, the agreement is quite good. Averaging more than 100 data points, the agreement becomes better than 1°, and east–west tilts as well as north–south tilts at low altitudes average out to less than 1° as expected from the slow wind variations at those altitudes. Also, average pitch and

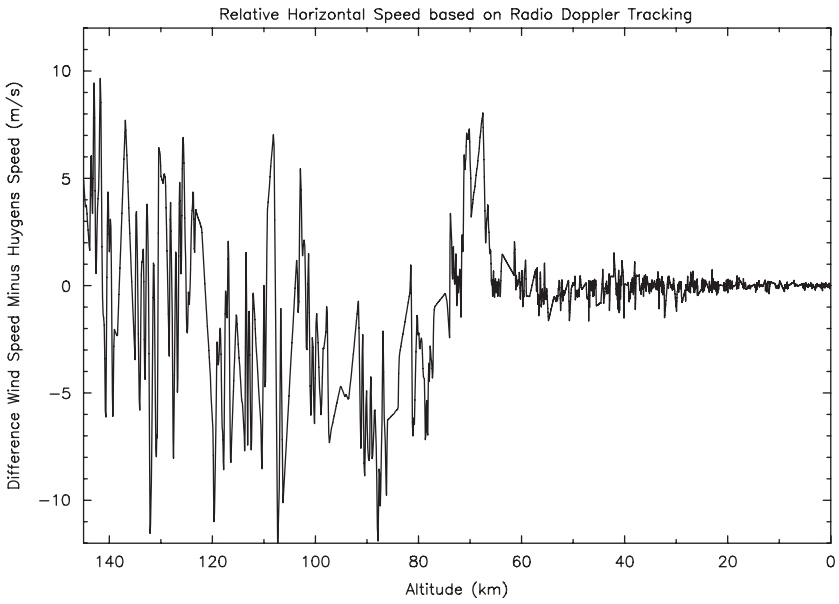

Fig. 26. Difference between zonal wind speed and zonal Huygens speed. A positive value means that Huygens moves west with respect to the atmosphere. None of the observed structure was expected.

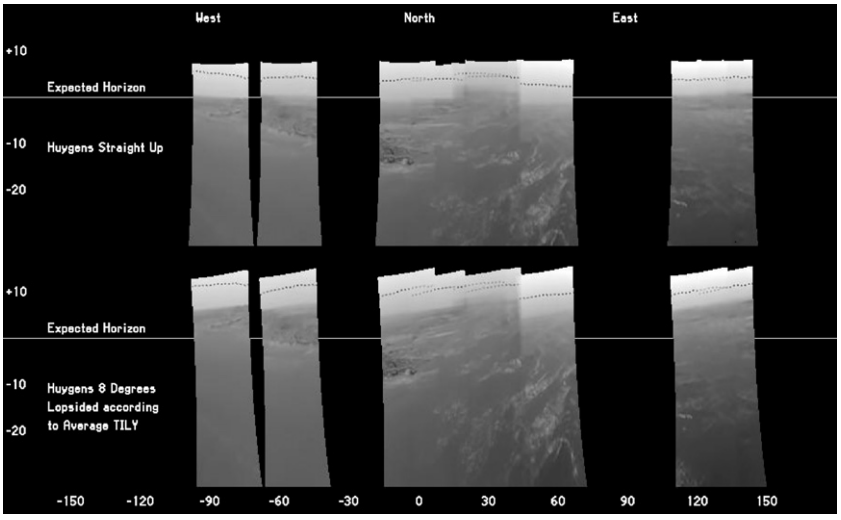

Fig. 27. The last nine SLI images before landing based on the assumption of no tilt of Huygens (top) and for a constant tilt of 8° according to TIL-Y data (bottom). As described in the text, the images are inconsistent with a tilt near 8°.

average roll angles of Table 2 are 0.2° and −0.3°, respectively, estimated to be reliable to 1°, indicating that nothing asymmetric happened during the descent, such as one of the three ropes supporting Huygens being of different length that the other two.

On the other hand, only one of the SSP tilt sensors (TIL-X) recorded averages close to zero, while the other one (TIL-Y) had an average near −8° (Lorenz, private communication). Zarnecki et al. (2005) concluded from this offset that Huygens was tilted on one side throughout the descent on both parachutes, and even after landing to the same side by a similar amount. Because of our result, we disagree with this interpretation and suspect an offset in the data of TIL-Y, since we cannot imagine any mechanism which would give straight images for a lopsided Huygens.

An example is displayed in Fig. 27, where the last nine SLI images before landing are shown at their azimuth and vertically aligned with the expected location of the theoretical horizon for a spherical Titan. In the top part of the figure, Huygens is assumed to have zero tilt. The horizon in each image lines up more or less at the expected location, except for some shifts of 1–2°. We interpret this as tilt of Huygens, since our other data also indicate a typical tilt of Huygens of 1–2° at low altitudes. The dotted lines in the sky in Fig. 27 are isophotes. They are expected to be roughly parallel to the horizon except for a brightening of the sky toward the Sun and above bright surface features,

where the sky got illuminated by the ground. The latter reason probably applies to the tilted isophote looking left, because the surface mosaic shows a significant brightness gradient with the correct sign.

The bottom part of Fig. 27 shows the same scene with the assumption of Huygens constantly tilted by 8° according to the average TIL-Y data. In all images, the apparent horizon is about 7° above the expected one, indicating the Huygens landing site would be a low point with the terrain sloping up by 7° in most directions. Images taken at higher altitudes taken show a similar angle, indicating that the horizon must be far away, on the order of 100 km. Photometric modeling of the transition zone at the apparent horizon combined with our estimation of the haze optical depth (Tomasko et al., private communication) also points to a distance of the horizon on the order of 100 km. The same number is expected for a spherical Titan for altitudes of one or a few kilometers. A 100 km distance taken together with the 7° slope would indicate that the horizon would be at least 10 km higher than the landing site. This is completely inconsistent with Cassini radar observations of the Huygens landing site area during the T8 flyby, which found the highest mountain peaks some 600 m high (Lunine et al., 2007). A horizon raised by 7° looking straight west (Fig. 27) is also inconsistent with the timing of the loss of signal to Cassini, which indicated that Cassini still received data when it was 0.5° below the theoretical horizon of Huygens (Pérez-Ayúcar et al., 2006). With the refraction of 1.0°, the upper limit of the apparent horizon is 0.5° above the theoretical horizon, well below the 7° needed for the lower part of Fig. 27. This result is consistent with our mosaic near the landing site, which looks more featureless (and thus possibly flat) toward the west than toward the south, where we found the apparent horizon elevated by 1.5°.

In all observed directions in the bottom part of Fig. 27, the horizon is sloping upward toward the right by a 5° slope. With so much topography around the landing site, one would expect that a few of the nine images may have caught some topographic feature at the horizon, but the horizon seems to be a perfectly straight line in all images. Furthermore, all the isophotes in the sky are sloping up toward the right. This would be theoretically possible if the isophotes were sloping the opposite way at azimuths which were not observed in the last SLI images before landing. However, images taking at higher altitudes show the same slope of the isophotes even at those azimuths not observed during the very end of the descent. It is simply impossible that isophotes are sloping the same way for all azimuths.

During our analysis of DISR data, we have encountered other results which are inconsistent with Huygens descending lopsided by 8° as indicated by TIL-Y, but the discussion of the previous paragraph should be sufficiently convincing, that Huygens was not consistently lopsided, and that the offset of TIL-Y is probably an instrumental effect.

10.4. Attitude on short time scales and turbulence

Section 7 presented data, suggesting that Huygens was swinging rapidly, typically 10°/s, even more than the upper limit design of 6°/s. Only during the main-parachute phase was the probe swinging slowly, roughly consistent with the swinging speeds expected from the large horizontal accelerations. On the stabilizer, the actual swinging speeds

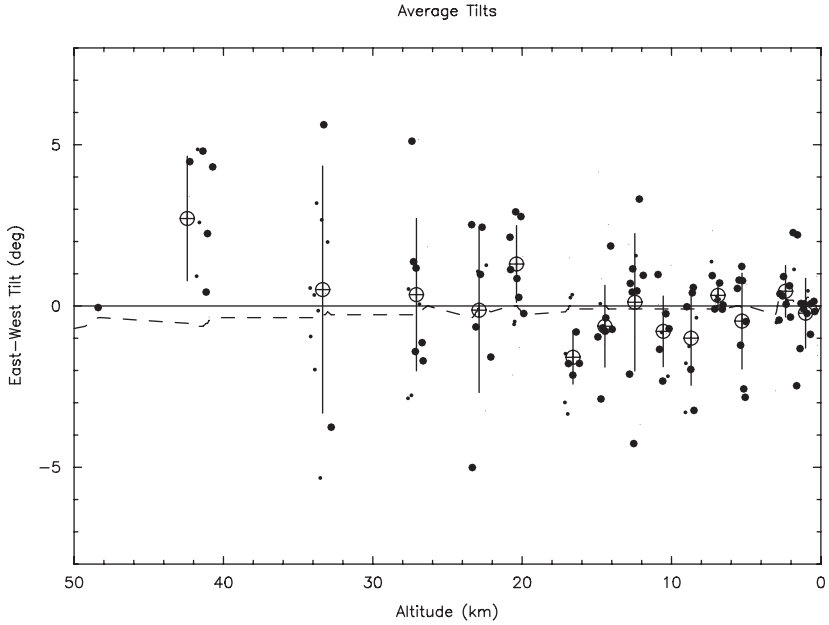

Fig. 28. Huygens tilt at the time of image exposures. Large dots indicate HRI exposures with more accurate data than MRI and SLI exposures (small dots). For each set of 12 exposures, the average (crossed circle) and standard deviation (vertical line) is shown. Images taken above 40 km altitude show little detail, and their data may be very uncertain. The dashed curve is the expected tilt due to a decreasing wind speed toward the surface. A positive tilt means that the axis of Huygens points to the east of the zenith.

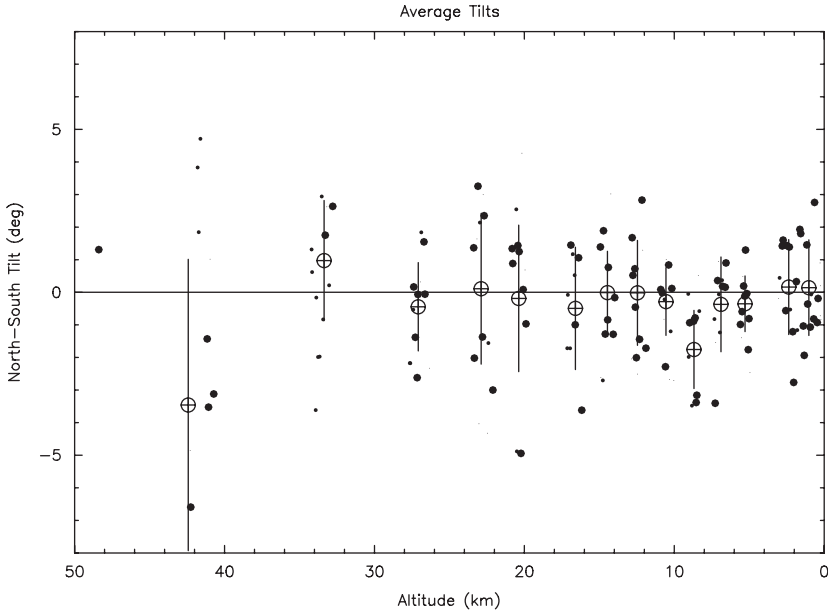

Fig. 29. Same as Fig. 28, except the north–south component of the tilt is shown. A positive tilt means that the axis of Huygens points to the north of the zenith.

were at least an order of magnitude larger than the expected swinging speeds from horizontal accelerations. These large swinging speeds must have come from the fast swing mode of 1.2 s period, where the center of Huygens and of the parachute remains essentially stationary, with the lines in between swinging. Our data suggest that this swinging occurred constantly, without significant periods of rest, although the amplitude of the swing may have varied strongly (Figs. 28 and 29).

On the main parachute, the large wind speed variations did not cause high swing rates. On the stabilizer, wind speed variations and tilts of Huygens decreased, yet the swing rates increased significantly. This may indicate that the high swing rates were not caused by irregularities in the wind speed profile, but by something like turbulence generated by Huygens.

It is interesting to note that rotation irregularities show the same distribution as the high swing rates: they are absent during the main-parachute phase, they start within a minute of the parachute exchange, and they remain present throughout the rest of the descent. Both could be excited by the same mechanism.

The large swing rates caused the Sun Sensor to partially fail and made it impossible to predict the tilt 0.1 s before or after an observation with a recorded tilt. This harmed individual data points, but not the whole data set due to the large number of data points taken. Again, the DISR data are thus less user-friendly, but the entire science goal still can be obtained.

Acknowledgments

Support for this work was provided by NASA through JPL contract numbers 961160 and 1279652. Several parts of this investigation were made possible by substantial help from Ralph Lorenz, who also suggested many improvements to the manuscript. Additional very useful comments came from Mark Leese and two anonymous reviewers.

Appendix A. Archive information

The data for this work were archived at the NASA Planetary Data System and the ESA Planetary System Archive. Most of the data used here came from the DISR instrument. They were archived by Tomasko in 2007 under HP-SSA-DISR-2-3-EDR-RDR-V1.0.

The DTWG#4 release was archived by Kazeminjad in 2006 under HP-SSA-DTWG-6-TRAJECTORY-V1.0.

The Huygens housekeeping data were archived by Witasse in 2007 under HP-SSA-HK-2/3-V1.0.

Appendix B. Analytical reflectivity function

Given here is an analytical function, which approximates the brightness seen from the Huygens imagers for any combination of altitude, azimuth, and nadir angle. The input variables are the altitude h (km), the azimuth A measured clockwise from the solar azimuth, the nadir angle β measured from the nadir, and the solar zenith angle z measured from the zenith (Table 6). Where the path to the surface is less than about 60 km, the brightness I/F_s, the brightness of the surface when vertically viewed from close distance, is also required. Typical values for I/F_s are 0.025 for dark lakebeds and 0.03–0.04 for bright highlands. The output is the I/F where I is the intensity and πF is the solar flux for the passband of the imagers at the top of Titan's atmosphere (15 W/m^2). This approximation is good to 2% rms.

Table 6
Angular position of the sun

T0	ZA	Az
100 s	39.3°	113.1
400	38.7	113.3
700	38.0	113.6
1000	37.5	113.8
2000	36.8	114.2
3000	35.9	114.5
5000	35.0	114.9
7000	34.5	115.1
8870	34.0	115.3
13,000	33.1	115.9

Note: MT, mission time; ZA, solar zenith angle; Az, solar azimuth, eastward of north.

First, we calculate the phase angle α through

$$\cos\alpha = \cos z\cos\beta - \sin z\sin\beta\cos A.$$

Next we calculate the nadir angle of the theoretical horizon β_h through

$$\sin\beta_h = 1/(1 + h/2575).$$

If $\beta_h > \beta$ we calculate

$$S = I/F_s,$$

$$d = \tan(\beta_h - \beta),$$

$$D = \sqrt{(5150h)},$$

$$\tau_h = 0.04\{D - 2575d[\sqrt{(1 + D/d/1287.5)} - 1]\}\sqrt{(1 + d^2)}.$$

Note that d and D are auxiliary parameters to calculate the distance between the probe and the viewed surface point in kilometers, which is the whole term after "0.04" in the previous equation. The numbers 5150, 2575, and 1287.5 come from Titan's assumed radius of 2575 km.

If $\beta_h < \beta$ we calculate

$$S = 0,$$

$$\tau_h = 2.5\times10^{-9}\sum\{3075 - \sqrt{[(2575 + h - (50*n - 25)\cos\beta)^2 + (50*n - 25)^2\sin^2\beta]}\}^3,$$

where the sum is taken over $n = 1, 2, 3, \ldots$ as long as the whole summand remains positive.

After the evaluation of S and τ_h, an approximation of the haze optical depth, we continue with the evaluation of a haze-brightness term

$$B = -1.429 - 0.065\cos\beta - 0.279\cos^2\beta + (0.108 - 3.18\cos\beta + 0.88\cos^2\beta)\exp(-h/45) + (-1.725 + 1.49\cos\beta + 2.1\cos^2\beta)\exp(-h/22.5) - 0.85\cos^2\beta\exp(-h/15) + 10^{-9}[h\,\mathrm{DIM}(155, h)]^2,$$

where $\mathrm{DIM}(a, b) = a - b$ if $a > b$ and zero otherwise.

We continue with

$$H = 70 + \mathrm{DIM}(h, 70) - \mathrm{DIM}(h, 132),$$

$$P = [0.51 + 6\times10^{-8}(H - 70)^2 + (120 - H)(140 - H)] \times \exp[-2.58\exp(2.25\cos\beta - h/20)](0.55 - \cos\alpha)^2 + 0.0162\,\mathrm{DIM}(0.55, \cos\alpha)^{10}.$$

P is an adjustment of the haze brightness valid for phase angles less than 140°.

Finally

$$I/F = \exp(B + P)\,[1 - \exp(-\tau_h)] + S\exp(-\tau_h).$$

References

Bird, M.K., Allison, M., Asmar, S.W.D., Atkinson, H., Avruch, M., Dutta-Roy, R., Dzierma, Y., Edenhofer, P., Folkner, W.M., Gurvits, L.I., Johnston, D.V., Plettemeier, D., Pogrebenko, S.V., Preston, R.A., Tyler, G.L., 2005. The vertical profile of winds on Titan. Nature 438, 800–802.

Fulchignoni, M., Ferri, F., Angrilli, F., Ball, A.J., Bar-Nun, A., Barucci, M.A., Bettanini, C., Bianchini, G., Borucki, W., Colombatti, G., Coradini, M., Coustenis, A., Debei, S., Falkner, P., Fanti, G., Flamini, E., Gaborit, V., Grard, R., Hamelin, M., Harri, A.M., Hathi, B., Jernej, I., Leese, M.R., Lehto, A., Lion Stoppato, P.F., López-Moreno, J.J., Mäkinen, T., McDonnell, J.A.M., McKay, C.P., Molina-Cuberos, G., Neubauer, F.M., Pirronello, V., Rodrigo, R., Saggin, B., Schwingenschuh, K., Seiff, A., Simões, F., Svedhem, H., Tokano, T., Towner, M.C., Trautner, R., Withers, P., Zarnecki, J.C., 2005. In situ measurements of the physical characteristics of Titan's environment. Nature 438, 785–791.

Kazeminejad, B., Pérez-Ayúcar, M., Lebreton, J.-P., Sanchez-Nogales, M., Belló-Mora, M., Strange, N., Roth, D., Popken, L., Clausen, K., Couzin, P., 2004. Simulation and analysis of the revised Huygens probe entry and descent trajectory and radio link modeling. Planet. Space Sci. 52, 799–814.

Kazeminejad, B., Atkinson, D.H., Pérez-Ayúcar, M., Lebreton, J.-P., Huygens Descent Trajectory Working Group, 2007. Huygens' entry and descent through Titan's atmosphere. Planet. Space Sci., this issue.

Lebreton, J.-P., Witasse, O., Sollazzo, C., Blancquaert, T., Couzin, P., Schipper, A.-M., Jones, J.B., Matson, D.L., Gurvits, L.I., Atkinson, D.H., Kazeminejad, B., Pérez-Ayúcar, M., 2005. An overview of the descent and landing of the Huygens probe on Titan. Nature 438, 758–764.

Lorenz, R.D., 1993. The life, death and afterlife of a raindrop on Titan. Planet. Space Sci. 41, 647–655.

Lorenz, R.D., 2006. Thermal interaction of the Huygens probe with the Titan environment: surface windspeed constraint. Icarus 182, 559–566.

Lunine, J., et al., 2007. Cassini radar's third and fourth looks at Titan. Icarus, submitted for publication.

Niemann, H.B., Atreya, S.K., Bauer, S.J., Carignan, G.R., Demick, J.E., Frost, R.L., Gautier, D., Haberman, J.A., Harpold, D.N., Hunten, D.M., Israel, G., Junine, J.I., Kasprzak, W.T., Owen, T.C., Paulkovich, M., Raulin, F., Raaen, E., Way, S.H., 2005. The abundances of constituents of Titan's atmosphere from the GCMS instrument on the Huygens probe. Nature 438, 779–784.

Pérez-Ayúcar, M., Lorenz, R.D., Floury, N., Prieto-Cerdero, R., Lebreton, J.-P., 2006. Bistatic observations of Titan's surface with the Huygens probe radio signal. J. Geophys. Res. Planets 111, E07001.

Tokano, T., McKay, C.P., Neubauer, F.M., Atreya, S.K., Ferri, F., Fulchignoni, M., Niemann, H.B., 2006. Methane drizzle on Titan. Nature 442, 432–435.

Tomasko, M.G., Buchhauser, D., Bushroe, M., Dafoe, L.E., Doose, L.R., Eibl, A., Fellows, C., McFarlane, E., Prout, G.M., Pringle, M.J., Rizk, B., See, C., Smith, P.H., Tsetsenekos, K., 2002. The Descent Imager/Spectral Radiometer (DISR) experiment on the Huygens entry probe of Titan. Space Sci. Rev. 104, 469–551.

Tomasko, M.G., Archinal, B., Becker, T., Bézard, B., Bushroe, M., Combes, M., Cook, D., Coustenis, A., deBergh, C., Dafoe, L.E., Doose, L., Douté, S., Eibl, A., Engel, S., Gliem, F., Grieger, B., Holso, K., Howington-Kraus, E., Karkoschka, E., Keller, H.U., Kirk, R., Kramm, R., Küppers, M., Lanagan, P., Lellouch, E., Lemmon, M., Lunine, J., McFarlane, E., Moores, J., Prout, G.M., Rizk, B., Rosiek, M., Rueffer, P., Schröder, S.E., Schmitt, B., See, C., Smith, P., Soderblom, L., Thomas, N., West, R., 2005. Rain, winds and haze during the Huygens probe's descent to Titan's surface. Nature 438, 765–778.

Tomasko 2007. HP-SSA-DISR-2-3-EDR-RDR-V1.0, NASA Planetary Data System & ESA Planetary Science Archive.

Zarnecki, J.C., Leese, M.R., Hathi, B., Ball, A.J., Hagermann, A., Towner, M.C., Lorenz, R.D., McDonnell, A.M., Green, S.F., Patel, M.R., Ringrose, T.J., Rosenberg, P.D., Atkinson, K.R., Paton, M.D., Banaszkiewicz, M., Clark, B.C., Ferri, F., Fulchignoni, M., Ghafoor, N.A.L., Kargl, G., Svedhem, H., Delderfield, J., Grande, M., Parker, D.J., Challenor, P.G., Geake, J.E., 2005. A soft solid surface on Titan as revealed by the Huygens surface science package. Nature 438, 792–795.